

The Pennsylvania State University
The Graduate School
College of Earth and Mineral Sciences

**AN EXPERIMENTAL STUDY OF LITHIUM PARTITIONING BETWEEN
OLIVINE AND DIOPSIDE AT UPPER MANTLE CONDITIONS**

A Thesis in
Geosciences
by
Jessica L. Yakob

© 2011 Jessica L. Yakob

Submitted in Partial Fulfillment
of the Requirements
for the Degree of

Master of Science

May 2011

The thesis of Jessica L. Yakob was reviewed and approved* by the following:

Maureen D. Feineman
Assistant Professor of Geosciences
Thesis Advisor

David H. Egger
Emeritus Professor of Geosciences

Peter J. Heaney
Professor of Geosciences

James D. Kubicki
Associate Professor of Geoscience

Sarah C. Penniston-Dorland
Assistant Professor of Geology
University of Maryland, College Park, Maryland
Special Signatory

Chris J. Marone
Professor of Geosciences
Associate Department Head of Graduate Programs

*Signatures are on file in the Graduate School

ABSTRACT

The mantle makes up more than 75% of Earth by volume. This vast layer of our planet drives plate tectonics as it redistributes heat and mass with large-scale convection cycles. While analytical geochemistry and numerical modeling have enabled researchers to uncover many properties of Earth's dynamic mantle, our understanding is not yet complete. Geochemical studies of mantle-derived materials such as basalts and peridotite xenoliths have revealed that the mantle is compositionally heterogeneous on a large scale. These heterogeneities offer insights into the controlling factors in mantle processes. The use of lithium as a geochemical tracer holds promise for mantle studies due to the large variation in Li isotope ratios in natural materials and the structural compatibility of Li in mantle minerals. High lithium diffusion rates coupled with the potential for isotope fractionation during diffusion complicate the interpretation of lithium signals in mantle materials, but create the opportunity to discern the *rates* of mantle processes. Minerals such as olivine and diopside, found in mantle xenoliths from diverse localities, exhibit unexpectedly large differences in $^7\text{Li}/^6\text{Li}$ ratios, usually with lighter Li found in the diopsides. Because ^6Li diffuses faster than ^7Li , bulk lithium exchange between two phases could result in dynamic isotopic fractionation, with the receiving phase becoming lighter and the donating phase becoming heavier. Thus if Li becomes more compatible in diopside upon cooling, that is, if $D_{\text{Li}}^{(\text{ol/di})}$ is temperature-dependent, the diffusive exchange of Li will generate temporary ^6Li enrichment in diopside and depletion in olivine. This thesis explores the hypothesis that a temperature-dependent partition coefficient for lithium between olivine and diopside is responsible for the divergent lithium isotope ratios measured between these two minerals in mantle xenoliths.

The conditions causing the different isotope ratios between phases can be inferred by comparing Li concentrations and isotope ratios measured in natural samples to experimentally determined equilibrium distributions between olivine and diopside for various temperatures and pressures. However, the equilibrium elemental distributions and isotope fractionation factors for lithium in mantle minerals at high temperature and pressure are largely unknown. Experiments were conducted using a piston cylinder apparatus at 700 °C, 900 °C, and 1100 °C and 1.5 GPa (1-10 days) to determine $D_{\text{Li}}^{(\text{ol/di})}$. San Carlos olivine and De Kalb diopside were finely ground for starting materials, and Milli-Q water with 100 ppm Li and 500 ppm Ba served as the lithium source. Lithium concentrations in olivine and diopside from experiments held for 1, 3, 5, and 10 days were determined by laser ablation inductively coupled plasma mass spectrometry. Partition coefficients ($D_{\text{Li}}^{(\text{ol/di})}$) from experiments conducted at 700-1100 °C are, within error, the same, $2.2 (\pm 0.3)$, suggesting that $D_{\text{Li}}^{(\text{ol/di})}$ is not temperature dependent. These fall in the lower portion of the range, $D = 2-7$, of limited previous measurements.

TABLE OF CONTENTS

List of Tables	v
List of Figures	vi
Acknowledgements.....	ix
1 INTRODUCTION.....	1
1.1 Lithium as a Geochemical Tracer.....	1
1.2 Purpose of Study.....	4
2 EXPERIMENTAL AND ANALYTICAL METHODS.....	7
2.1 Starting Materials.....	7
2.2 Sample Preparation and Piston-Cylinder Experiments.....	8
2.3 Analytical Methods.....	9
3 RESULTS.....	15
3.1 Analytical Results.....	15
3.2 Partition Coefficients.....	16
4 DISCUSSION.....	26
4.1 Assessment of Equilibrium.....	26
4.2 Trace Element Partitioning Theory and Mechanisms of Lithium Incorporation.....	27
4.3 Comparison to Other Studies of Lithium Partitioning.....	30
4.4 Implications for Observed $\delta^7\text{Li}$ in Mantle Xenoliths.....	31
5 CONCLUSIONS.....	38
6 FAILED CARBONATE EXPERIMENTS: LESSONS LEARNED.....	39
6.1 Motivation.....	39
6.2 Methods	39
6.3 Experimental Results.....	42
6.4 Discussion.....	43
6.5 Conclusions.....	44
REFERENCES.....	51

LIST OF TABLES

Table 2.1. Summary of samples and experimental conditions for olivine-diopside partitioning experiments	13
Table 3.1. Major element concentrations of starting material and run product diopsides (DKD3, di), olivines (SCO2, ol), and enstatite (en) using EPMA (2 σ in parentheses)....	21
Table 3.2. Trace element concentrations of starting material and run product diopsides (DKD, di) and olivines (SCO, ol), and enstatite (en) using LA-ICP-MS (2 σ in parentheses).....	22
Table 3.3. Partition coefficients ($D_{Li}^{(ol/di)}$) for run products (2 σ in parentheses). Italicized samples have not approached equilibrium.....	23
Table 6.1. Summary of samples and experimental conditions for LiBaC experiments....	46
Table 6.2. Summary of MC-ICP-MS analyses for starting materials, run product olivines, and run product CO ₃ dissolved in HCl for LiBaC experiments.....	47
Table 6.3. Summary of LA-ICP-MS results for starting materials and run products from LiBaC experiments (2 σ error in parentheses).....	48
Table 6.4. Summary of SIMS results for starting materials and run products from LiBaC experiments (2 σ error in parentheses).....	48

LIST OF FIGURES

Figure 1.1. Lithium isotopic composition of various reservoirs, Figure 1 from Tang <i>et al.</i> , 2007.....	6
Figure 1.2. Summary of published $\delta^7\text{Li}$ in olivine and clinopyroxene from mantle xenoliths. Circles are samples reported by Seitz <i>et al.</i> , 2004. Squares are samples reported by Rudnick and Ionov, 2007. Squares are samples reported by Jeffcoate <i>et al.</i> , 2007. Triangles are samples reported by Ionov and Seitz, 2008. Gray line is a 1:1 trendline, representing $\alpha_{\text{Li}}^{\text{ol-di}} = 1$	6
Figure 2.1. Sample assembly used for piston-cylinder experiments. Left, schematic of sample assembly. Right, photograph of components for the sample assembly (thermocouple not included). Not to scale.....	12
Figure 2.2. Design of piston-cylinder apparatus. Left, schematic of piston-cylinder apparatus, based on the design of Boyd and England, 1960. Right, photograph of the piston-cylinder apparatus used for this study.....	12
Figure 2.3. Example of a typical standard spectrum used for LA-ICP-MS sample-standard bracketing.....	14
Figure 3.1. Backscattered SEM image of run product Li-27 (1100 °C, 5 days) grains mounted in epoxy. The brightest objects are remnants of the Ni crucible or Pt capsule that contained the charge. The darker gray grains are olivines and the lighter gray grains are diopsides. Smaller grains are quench products, consisting primarily of fused K-Al-silicate spherules.....	17
Figure 3.2. Backscattered SEM image of run product Li-43 (900 °C, 5 days) grains mounted in epoxy. The darker gray grains are olivines and the lighter gray grains are diopsides. Smaller grains are quench products.....	18
Figure 3.3. Backscattered SEM image of run product Li-39 (700 °C, 3 days) grains mounted in epoxy. The darker gray grains are olivines and the lighter gray grains are diopsides. Feathery crystals are quench products. The darker gray quench needles are primarily orthopyroxene, and the brighter quench needles are K-Al-silicates that rarely contain Ca and Ba.....	19
Figure 3.4. Backscattered SEM image of run product Li-37 (700 °C, 10 days) grains mounted in epoxy. The darker gray grains are either olivine or enstatite and the lighter gray grains are diopsides. Smaller grains are quench products, consisting primarily of feathery orthopyroxene needles. The box magnifies enstatite grain 1a.....	20

Figure 3.5. Li concentrations in olivine (solid line) and diopside (dashed line) for starting materials and the three temperature series investigated. A) Li concentrations for starting materials and 1100 °C experiments at 1, 3, and 5 days. B) Li concentrations for starting materials, 1100 °C 1 day treatment, and 900 °C experiments at 1, 3, and 5 days. C) Li concentrations for starting materials, 1100 °C 1 day treatment, and 700 °C experiments at 1, 3, 5, and 10 days.....24

Figure 3.6. Lithium concentrations in olivine versus lithium concentrations in diopside for the run product grains that are interpreted to have approached equilibrium partitioning. Data are plotted for experiments lasting 5 and 10 days at 700 °C, 3 and 5 days at 900 °C, and 3 and 5 days at 1100 °C. The slope of the trendline indicates the partition coefficient ($D_{Li}^{(ol/di)}$) is ~2.3 for all temperature series investigated in this study.....25

Figure 3.7. Measured partition coefficients ($D_{Li}^{(ol/di)}$) from experimental run products plotted versus temperature of experiment. Data are plotted for experiments lasting 5 and 10 days at 700 °C, 3 and 5 days at 900 °C, and 3 and 5 days at 1100 °C. Error bars represent 1 σ deviations for each measured D. Values of measured $D_{Li}^{(ol/di)}$ for plotted experiments fall between 2 and 2.4, with an average of 2.2 (\pm 0.3).....25

Figure 4.1. Measured partition coefficients ($D_{Li}^{(ol/di)}$) are plotted against experiment duration (days). Error bars are 1 σ deviations. As the 700 °C and 900°C series each endured a preliminary day at 1100 °C (for enhanced grain growth), at zero days the 700 °C and 900 °C series are assumed to have a partition coefficient equal to that observed for the 1 day, 1100 °C experiment. The 1100 °C series and 900 °C series are interpreted to approach equilibrium after three days and the 700 °C series is interpreted to approach equilibrium after five days.....36

Figure 4.2. Plot comparing Li concentrations in olivine and diopside found in this study to published data. Open circles are data from this study, open diamonds are experimental studies with aqueous fluid, bold open diamonds showing experiments containing both olivine and diopside (Caciagli-Warman, 2010), open triangles are experimental studies with carbonate melt (Blundy and Dalton, 2000), and open squares are experimental studies with silicate melt (Brenan *et al.*, 1998a), and filled circles are natural mantle xenolith samples (Seitz and Woodland, 2000; Paquin and Altherr, 2002; Woodland *et al.*, 2004). The data tend to fall on a linear 2.2:1 trendline (gray line) with some of the mantle xenolith samples deviating significantly. Sp = spinel, Gt = garnet.....36

Figure 4.3. Arrhenius plot of Li diffusion coefficients measured for clinopyroxene (Coogan *et al.*, 2005) and olivine (Dohmen *et al.*, 2010). Two diffusion mechanisms for Li diffusion in olivine are plotted (interstitial site and octahedrally-coordinated metal site). The metal site is expected to control Li diffusion in olivine. The data show that Li diffuses faster in clinopyroxene (by one or two orders of magnitude) than metal site Li diffusion in olivine.....37

Figure 6.1. Schematic of sample assembly used for LiBaC experiments with the piston-cylinder.....46

Figure 6.2. Diopside and olivine SIMS results for Li vs. Ba concentrations ($\mu\text{g/g}$). Diopside data presented on left, olivine data presented on right. Open circles and squares represent the experiment that contained 20 ppm Li in the LiBaC powder (LiBaC 3). Closed circles and squares had 200 ppm Li in the LiBaC powder (LiBaC 2). Square symbols represent the 24 hour experiment and circles are the 4 hour experiment. The open diamonds represent analyses of starting material minerals, and the black open diamond represents the average Li and Ba concentrations for the starting materials. The red lines are mixing lines whose end-members are the starting material mineral and the LiBaC powder used for the particular experiment. Inclusions of the LiBaC powder are evidenced by the data points having Ba concentrations greater than 15 ppm. The data do not follow the red mixing curves, but instead indicate interaction with a partial-melt of BaCO_3 and LiCO_3 , for which the Li concentration is not numerically quantified but is much higher than the original powder Li concentration.....49

Figure 6.3. Run product images showing cracks and inclusions containing partially molten LiBaC powder in a) olivine and b) diopside.....50

ACKNOWLEDGMENTS

I'd like to first acknowledge my advisor, Maureen Feineman, for her infinite patience and guidance throughout my program. She has taught me many valuable lessons, both professional and personal, and I am deeply grateful for all she has done for me. David Egger has played a major role in the success of this project, and I'd like to thank him for his help, his instruction, his questions, and his direction. Sarah Penniston-Dorland, from the University of Maryland, has been a fantastic collaborator, and I'd like to recognize her as my mentor away from PSU. Additionally, I acknowledge my committee members, Peter Heaney and Jim Kubicki for their helpful input throughout my time at Penn State.

This research was supported in part by

- NSF grant (EAR-0810129) and the E. Willard and Ruby S. Miller Fellowship, College of Earth and Mineral Sciences, PSU, awarded to Maureen Feineman.
- NSF grant (EAR-0911100) awarded to Sarah Penniston-Dorland.

Special thanks go to Richard Ash, Philip Piccoli, Waleska Castro, Mark Angelone, John Cantolina, Eizo Nakamura, Tsutomu Ota, Takuya Kunihiro, Steve Swavely, and Brian LeVay for their assistance regarding this project.

Finally, I could not have completed this project without the support of friends and family. Their encouragement and tolerance has been crucial to my success. Mom, Dad, Ryan, Kevin, Tim, TJ, Cici, Matt...thank you.

1 Introduction

1.1 Lithium as a Geochemical Tracer

Lithium (Li) has two stable isotopes, ${}^6\text{Li}$ and ${}^7\text{Li}$ (relative mass difference ~16%), with 92.5% of Earth's lithium budget present as ${}^7\text{Li}$. Because of the large isotopic mass difference, lithium is particularly susceptible to mass-dependent isotope fractionation, which is observed for natural samples and summarized by Figure 1 from Tang *et al.* (2007) (Figure 1.1). Lithium isotope ratios are commonly presented using delta notation ($\delta^7\text{Li} = [({}^7\text{Li}/{}^6\text{Li})_{\text{sample}}/({}^7\text{Li}/{}^6\text{Li})_{\text{standard}}] - 1] \times 1000$), which compares the sample to a standard and is reported in permil (‰). For two phases of interest, a comparison of their isotope ratios can be made using the isotope fractionation factor, $\alpha_{\text{Li}}^{\text{A-B}} = ({}^7\text{Li}/{}^6\text{Li})_{\text{A}}/({}^7\text{Li}/{}^6\text{Li})_{\text{B}}$, which describes the fractionation between the two phases. As shown in Figure 1.1, there is expansive elemental and isotopic distribution of lithium in the Earth. This wide Li distribution offers a unique opportunity to describe crustal, marine, mantle, and meteoritic processes that cause lithium fractionation (Tomascak 2004; Tang *et al.*, 2007).

In the bulk continental crust, there is an estimated 18 parts per million (ppm) Li (Teng *et al.*, 2008) with 35 ± 11 ppm ($\delta^7\text{Li} = 0 \pm 2$ ‰) in the upper continental crust (Teng *et al.* 2004) and 8 ppm ($\delta^7\text{Li} = +2.5$ ‰) in the lower continental crust (Teng *et al.*, 2008). These values are compared to those for both fresh mid-ocean ridge basalts (MORBs), which have ~6 ppm Li ($\delta^7\text{Li} = +3.7$ ‰) (Ryan and Langmuir, 1987; Chan *et al.*, 1992; Tomascak *et al.*, 2008), and for lithospheric mantle estimates of 1-2 ppm ($\delta^7\text{Li} = +3.5$ ‰) (Seitz and Woodland, 2000; Jeffcoate *et al.*, 2007). The Li abundances in fresh MORBs and mantle are quite different than those for altered basalts, which have about 26 ppm Li ($\delta^7\text{Li} = +14$ ‰) (Chan *et al.*, 1992). The Li isotopic signatures for fresh MORB and mantle are very similar, but altered basalts have a much heavier $\delta^7\text{Li}$. The differences in the lithium signatures from each of these sources suggest a promising future for the use of lithium as a geochemical tracer, especially as lithium from altered oceanic crust and sediments derived from continental crust is introduced into the mantle during subduction.

The use of lithium as a geochemical tracer has substantially increased within the past twenty years, particularly for tracing ocean-crust-mantle interactions resulting from crustal recycling at subduction zones, such as seafloor alteration and arc magma generation. Chan *et al.* (1992) observed altered seafloor with heavy Li isotope compositions. These workers used Li isotopic composition ($\delta^7\text{Li}$) and Li content ([Li]) to define the extent of alteration of seafloor basalts, and they determined a best estimate of the isotopic fractionation factor ($\alpha = 1.019$) for seawater/alteration-minerals. Lithium measurements from island arc lavas may hold significant promise for understanding crustal recycling at subduction zones, although interpretation of these data is not always straightforward. Tomascak *et al.* (2000) interpret that Li is released from the subducting slab at shallow depths (~30 km, Benton *et al.*, 1999), such that mantle modification starts early in the subduction process, and that Li will likely remain sequestered in the mantle wedge due to inefficient convection. Forearc mantle that has been enriched in ^7Li carried by fluid from the dehydrating slab could be incorporated into the arc magma source regions (Zack *et al.* 2003). Cross-arc variation in Li observed by Leeman *et al.* (2004) is thought to indicate regions in the mantle wedge having different lithium signatures.

Lithium isotope fractionation observed during crystallization at 500-600°C in granitic systems (Tomascak *et al.*, 1995) led to studies of Li isotope fractionation during crystallization in mafic systems. However, measurements of $\delta^7\text{Li}$ in Hawaiian basalts from Kilauea Iki lava lake show no evidence for isotopic fractionation as a result of fractional crystallization, suggesting that the fractionation factor (α) for Li approaches one at higher temperatures (Tomascak *et al.*, 1999a). Fractionation of Li isotopes has been observed for the Trinity ophiolite, however the fractionation is credited to Li diffusion during mantle melting (Lundstrum *et al.*, 2005) as opposed to fractionation caused by magmatic differentiation.

Developments in experimental studies of Li and its isotopes have become increasingly important for interpreting observations in natural samples. Richter *et al.* (2003) showed experimentally that for silicate melts, the diffusion coefficient for lithium is orders of magnitude greater than the diffusion coefficients for other elements, including noble gases. Furthermore, their work documents the faster diffusion of ^6Li

with respect to ^7Li . The faster diffusion of the lighter isotope is expected due to kinetic effects (White 2009); the lighter isotope has to travel faster than the heavier isotope for a given energy, i.e. $\text{KE} = (1/2)mv^2$, where KE is kinetic energy, m is mass, and v is velocity. Because the diffusivity of ^6Li is 3% faster than that of ^7Li (Richter *et al.*, 2003), a bulk redistribution of lithium from one phase into another could fractionate the two isotopes (i.e., kinetic fractionation). Data from partitioning and diffusion experiments for lithium in diopside and plagioclase conducted by Coogan *et al.* (2005) were used to determine the cooling rate of a mid-ocean ridge sheeted dike complex. As both the diffusion rate and the equilibrium partitioning of Li between diopside and plagioclase are temperature dependent, the extent of Li exchange therefore relies on the rate of cooling (Coogan *et al.*, 2005).

Within the last decade, much focus of Li and its isotopes has turned to mantle xenoliths and the minerals composing them. Figure 1.2 shows a summary of the published $\delta^7\text{Li}$ values for olivines and pyroxenes from mantle xenoliths. Lithium distributions between olivines and pyroxenes in natural xenoliths from six continents measured by Seitz and Woodland (2000) suggest that Li partitioning between orthopyroxene, olivine, and clinopyroxene is effectively independent of temperature, pressure, and bulk chemistry. The authors concluded that metasomatized xenoliths generally display a disequilibrium distribution of lithium among minerals compared to unmetasomatized xenoliths. One possible mechanism for fractionating the isotopes of Li at high temperatures is by differential diffusion of ^6Li and ^7Li . Jeffcoate *et al.* (2007) investigated the isotopic fractionation of lithium for peridotite xenoliths and mafic melts, inferring that ^6Li diffuses faster than ^7Li , and propose that isotopic disequilibrium observed for xenoliths could be due to exchange with magmatic fluid during transport. Rudnick and Ionov (2007) demonstrated that within a single peridotite xenolith, significant lithium zoning was evident for clinopyroxenes whereas olivines had little zoning. They interpret that clinopyroxene preferentially sequesters lithium from a grain boundary fluid or melt and as a result increases the extent of isotopic disequilibrium.

In order to better understand the reason for observed isotopic disequilibrium, many researchers have investigated Li diffusivities and partitioning behavior for olivine

and clinopyroxene. Research by Parkinson *et al.* (2007) inferred relative rates of lithium diffusion in olivines and clinopyroxenes in primitive arc lavas using Li isotope profiles and residence times, referenced to the Fe-Mg diffusion rate in olivine (Li diffusion is 4-8x slower in olivine and 20-30x faster in clinopyroxene than Fe-Mg diffusion in olivine). The authors suggest that the inferred diffusion rates might explain observed isotopic disequilibrium between olivine and clinopyroxene, implying that minerals in mantle xenoliths interacting with host lavas during transport could exhibit marked differences in $\delta^7\text{Li}$ over the span of a few days. This result indicates lithium isotopes are well-suited for studying short term fluid-rock or melt-rock interactions immediately before and during eruption. A recent study by Dohmen *et al.* (2010) concerning the diffusion of lithium into olivine has identified three mechanisms of lithium incorporation into olivine (octahedrally coordinated Mg site, vacant octahedral site, and interstitial site), as well as the respective diffusion rates for the differing mechanisms. The Li diffusion rate in clinopyroxene reported by Coogan *et al.* (2005) is faster than the Li diffusivity found for the metal site in olivine, but is slower than the Li diffusivity found for the interstitial site in olivine (Dohmen *et al.*, 2010). An alternative explanation for the observed isotopic disequilibrium could be temperature-dependent partitioning between olivine and clinopyroxene. Ionov and Seitz (2008) concluded that duration of cooling (i.e. basaltic or pyroclastic eruption styles) could be the most important controlling factor on lithium partitioning between olivines and pyroxenes, suggesting that the distribution of lithium may change between the minerals so that Li becomes more compatible in clinopyroxene during cooling, with olivines retaining more ^7Li compared to the clinopyroxenes.

1.2 Purpose of Study

Olivine and diopside found in mantle xenoliths from diverse localities (Austria, Germany, Seitz *et al.*, 2004; USA, Seitz *et al.*, 2004; Jeffcoate *et al.*, 2007; Russia (Siberia), Seitz *et al.*, 2004; Jeffcoate *et al.*, 2007; Rudnick and Ionov, 2007; Ionov and Seitz, 2008; Mongolia, Jeffcoate *et al.*, 2007) exhibit large differences in $\delta^7\text{Li}$ even within a single hand sample, usually with lighter Li found in the diopsides (Seitz *et al.*, 2004; Jeffcoate *et al.*, 2007; Rudnick and Ionov, 2007; Ionov and Seitz, 2008). The conditions causing the apparent isotopic disequilibrium between mantle phases can be inferred by

comparing Li concentrations and isotope ratios measured in natural samples to experimentally determined partition coefficients and isotopic fractionation factors between olivine and diopside for various temperatures and pressures. However, the temperature dependence of the partition coefficients and isotope fractionation factors at mantle conditions has not been quantified.

At high temperatures, stable isotope fractionation is greatly reduced, hence the fractionation factor is expected to approach unity (Northrop and Clayton, 1966; Criss and Farquhar, 2008). While a deviation from unity of the isotopic fractionation factor with temperature could explain the observed ^6Li -enrichment in xenolith clinopyroxenes, a temperature dependence of the partition coefficient ($D_{\text{Li}}^{(\text{ol}/\text{cpx})} = [\text{Li}]_{\text{ol}}/[\text{Li}]_{\text{cpx}}$) could also explain the observed distribution of $\delta^7\text{Li}$. Because of its smaller mass, ^6Li diffuses faster than ^7Li , thus bulk lithium exchange between two phases could result in dynamic isotopic fractionation, with the receiving phase becoming lighter and the donating phase becoming heavier (Richter *et al.*, 2003). If Li becomes more compatible in diopside at lower temperatures, that is, if $D_{\text{Li}}^{(\text{ol}/\text{di})}$ is temperature-dependent, the diffusive exchange of Li upon cooling will generate temporary ^6Li enrichment in diopside and depletion in olivine. The temperature-sensitive nature of Li partitioning between plagioclase and clinopyroxene shown by Coogan and others (2005) further reinforces the possibility of a temperature control on Li partitioning between olivine and clinopyroxene as an explanation for observed $\delta^7\text{Li}$ trends in mantle xenoliths.

This study aims to determine the Li partition coefficients between olivine and diopside (a clinopyroxene end-member) for temperatures 700-1100 °C and pressures of 1.5 GPa using a piston-cylinder apparatus. The partition coefficients to be determined by this study will be useful for constraining models of Li isotope fractionation in natural systems (e.g., Gallagher and Elliott, 2009).

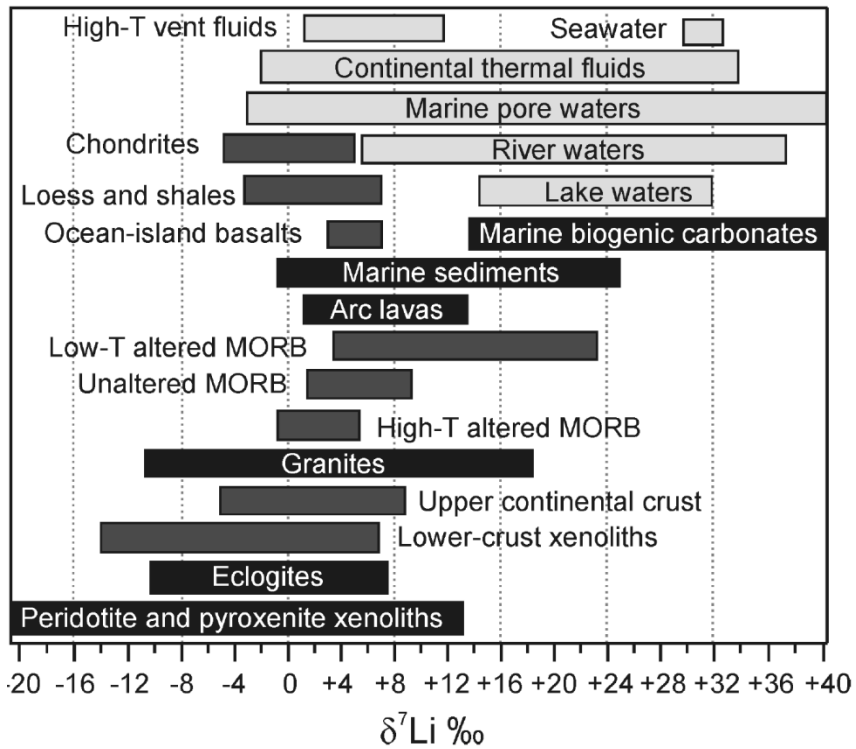


Figure 1.1. Lithium isotopic composition of various reservoirs, Figure 1 from Tang *et al.*, 2007.

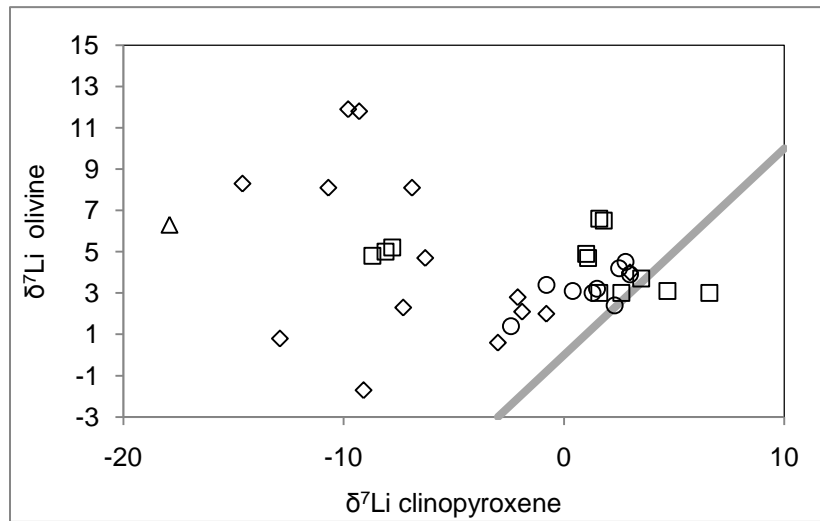


Figure 1.2. Summary of published $\delta^7\text{Li}$ in olivine and clinopyroxene from mantle xenoliths. Circles are samples reported by Seitz *et al.*, 2004. Squares are samples reported by Rudnick and Ionov, 2007. Squares are samples reported by Jeffcoate *et al.*, 2007. Triangles are samples reported by Ionov and Seitz, 2008. Gray line is a 1:1 trendline, representing $\alpha_{\text{Li}}^{\text{ol-di}} = 1$.

2 Experimental and Analytical Methods

2.1 Starting Materials

Natural crystals of olivine ($[\text{Mg}_{1.8}, \text{Fe}_{0.2}]\text{SiO}_4$) from San Carlos, Arizona and diopside ($\text{CaMgSi}_2\text{O}_6$) from DeKalb Junction, New York were chosen for use as starting materials for their close approximation to the Mg-endmembers of these phases. Mineral grains used for this study were cleaned in acetone then Milli-Q water in an ultrasonic bath before they were broken into mm-sized pieces using a hardened steel mortar and pestle. The olivines and diopsides were hand-picked under a stereo microscope to ensure the selection of grains free of alteration, inclusions, or surface contamination. The hand-picked grains were then ground in an agate mortar and pestle until the grains were $\leq 10 \mu\text{m}$. Powders of this smaller size were chosen with the expectation that during the hydrothermal experiments the powder particles having the smallest surface area would begin to dissolve into solution until the fluid becomes saturated, at which point deposition onto larger grains would occur, per the Ostwald ripening effect (Lifshitz and Slyozov, 1961; Steefel and Van Cappellen, 1990).

Other starting materials included natural orthoclase from Amelia, Virginia and Brazilian quartz, which were prepared using the same methods described above. Quartz and orthoclase are added to the experiments to prevent the incongruent dissolution of olivine and diopside as a result of high silica solubility in the fluid at run conditions. The relative proportion of starting materials was chosen based on high pressure and temperature experiments of the solubility of diopside and forsterite in water. Schneider and Eggler (1986) showed for the diopside-forsterite-water system at 1100 °C and 20 kbar that 3 wt. % solute is expected in the fluid. The solute is depleted in Mg and enriched in Si relative to the diopside starting material. Using this value as a guide, about 2 wt. % quartz and orthoclase was added to approach (but not overstep) saturation in the fluid.

Aqueous solutions of lithium were prepared from either lithium standard solutions or powdered Li_2CO_3 . For the first case, a standard solution containing 1000 ppm lithium in 2% HNO_3 was dried down and then picked up with Milli-Q water to produce a solution

(LiBaS1) with a final concentration of 100 ppm Li. In the second case, an aqueous solution with a controlled isotopic composition was prepared by dissolving a lithium carbonate isotope standard (IRMM-016) in Milli-Q water. The solution (LiBaS3) had 100 ppm Li with $\delta^7\text{Li} \approx 0$. Both solutions contained 500 ppm Ba, added as residue from an evaporated standard solution. Because Ba is strongly incompatible in olivine (Brenan *et al.*, 1995a), Ba was added to the starting solution with the intent to provide a means of assessing that Li was truly incorporated into the mineral structure (in which case Li would be detected in the absence of Ba), or whether Li was incorporated in fluid inclusions (in which case Li and Ba would increase together).

2.2 Sample Preparation and Piston-Cylinder Experiments

Procedures for the hydrothermal experiments are based on Ayers *et al.*, 1992. Platinum tubing (5 mm diameter) was cut 1.2 cm long, tri-welded on one end, and annealed before it was inserted into a ~1 cm long nickel crucible. Any protruding Pt was wrapped around the rim of the Ni crucible so that the entire rim was covered in Pt. Any excess Pt tubing was filed away. About 14.5 mg of minerals (olivine (7.5 mg), diopside (5 mg), orthoclase (1 mg), and quartz (1 mg)) were added to the capsule before it was filled with the prepared LiBaS solution (~100 mg) until a tension bubble was visible emerging from the capsule. A Pt disk (0.25 inch diameter) was placed over the capsule, followed by a Ni disk, followed by a thin disk of MgO.

Figure 2.1 shows the sample assembly for the hydrothermal LiBaS experiments. The sample is loaded into the Pt-lined Ni crucible, then the Pt disk is applied. The crucible is placed on top of the bottom MgO spacer, then the center MgO spacer is slid over the Ni crucible before the Ni disk and MgO disk are added. The graphite furnace is slid over the middle and bottom MgO spacers, then the top MgO spacer is added. Next, the Pyrex sleeve is slid over the graphite furnace. A small amount of contact cement is applied to the edges of the graphite plug, which is then inserted into the bottom of the Pyrex sleeve, just below the graphite furnace and the bottom MgO spacer. The salt cell is wrapped with the lead foil and inserted into the pressure plate, then the sample assembly is inserted into the salt cell (graphite plug side down). Next, the pyrophyllite sleeve is inserted on top of the salt cell and sample assembly, then the base plug is inserted inside

the pyrophyllite sleeve. Finally, the thermocouple is fed into the sample assembly for temperature control.

An end-loaded piston-cylinder apparatus was used to achieve the temperatures ranging from 700-1100°C and pressures of 1.5 GPa. The end load pressure was raised first, then the master ram pressure was brought about half-way to the final pressure. After testing thermocouple continuity, the temperature and pressure were brought up together to the run conditions. Figure 2.2 shows a schematic of the piston-cylinder. The temperature was maintained and measured during experiments using a Pt-Pt₉₀Rh₁₀ thermocouple. The run duration varied from 1 to 10 days. Experiments conducted at 700 °C and 900 °C were first held at 1100 °C for one day in order to encourage growth of olivine and diopside crystals. The experimental run conditions are summarized in Table 2.1.

Once the capsule was recovered and cleaned after the experiment, the final mass was compared to the mass before the run to verify fluid retention. The capsule was then sawed or filed open. The experimental run products were recovered after allowing residual water in the capsule to evaporate under a heat lamp. Run products were mounted in EpoThin® epoxy in either 1” phenolic or ¼” stainless steel rounds and allowed to cure overnight. A ratio of 2:1 resin:hardener was used. Once the epoxy cured, the mount was ground down to expose the run product crystals and polished using Metadi® diamond paste. In most cases, the mounts were polished to down to a 1 µm diamond polish.

2.3 Analytical Methods

Scanning Electron Microscope (SEM)

Polished grain mounts were carbon coated and analyzed with an FEI Quanta 200 environmental scanning electron microscope (ESEM) at the Materials Characterization Laboratory at Penn State University. Images were collected using secondary electrons (SE) and backscattered electrons (BSE). Back scattered electron imaging was used primarily for mapping a grain mount in order to distinguish olivine grains from diopside grains (based on contrast differences). Element mapping was completed using the INCA

software. Individual spectral patterns obtained with energy dispersive X-ray spectroscopy (EDS) were used to determine semi-quantitative compositions for particular grains of interest.

Electron Probe Micro-Analysis (EPMA)

Analysis of chemical composition by electron probe micro-analysis was conducted at the Electron Probe Microanalyzer Laboratory at the University of Maryland. Samples were polished with 1 μm diamond paste and were carbon coated before analysis. Starting materials and run products were analyzed for major and minor elemental concentrations using a JEOL JXA-8900 SuperProbe with a focused beam of 3 μm and accelerating voltage of 15 kV. A series of natural and synthetic olivines and pyroxenes were used as primary and secondary standards, and X-ray intensities were converted to concentrations using the CIT-ZAF correction scheme. Elemental concentrations were measured for Al, Ca, Cr, Fe, Mg, Mn, Ni, Si, Ti, and for some samples K and Na.

Laser Ablation Inductively Coupled Plasma Mass Spectrometry (LA-ICP-MS)

Analysis of Li concentrations by laser ablation inductively coupled plasma mass spectrometry (LA-ICP-MS) was conducted at the Isotope Geochemistry Laboratory at the University of Maryland. Starting materials and run products were analyzed for trace element concentrations using a New Wave UP213 Laser Ablation unit coupled with the Thermo-Finnigan Element 2 mass spectrometer. The New Wave UP213 employs a Neodymium-Yttrium-Aluminum-Garnet (Nd-YAG) ultraviolet laser (213 nm). Laser analyses were done using an output power of 2-3 J/cm^2 and a frequency of 7 Hz, with spot sizes ranging from 25-55 μm . Samples were ablated into a He stream and mixed with Ar gas before entering the Ar plasma torch of the ICP system. The spectrometer, a double focusing magnetic sector field ICP-MS, was operated at an accelerating voltage of 2000 V. Sample-standard bracketing was done to ensure accuracy; the standards were NIST 610, BHVO, BIR-1g, and/or BCR-2g. Every data collection sequence followed the template of four standards–twelve samples–four standards. Starting material and run product olivine and diopside were measured for ^6Li , ^7Li , ^{26}Mg , ^{28}Si , ^{43}Ca , ^{47}Ti , ^{49}Ti , ^{57}Fe , ^{60}Ni , ^{61}Ni , and ^{137}Ba .

Raw data from experimental run product analyses were reduced using an Excel spreadsheet with macros, LasyBoy3 V3.01, created by Joel Sparks of Boston University. Concentrations were calculated from background-corrected counts-per-second data using ^{26}Mg as a normalizing mass. Calibration lines were constructed from selected bracketing standards for each set of 12 unknowns. Figure 2.3 shows a typical spectrum for a standardizing sample used for sample-standard bracketing.

Sample Assembly

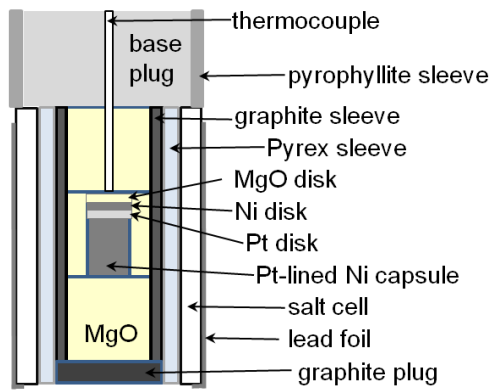
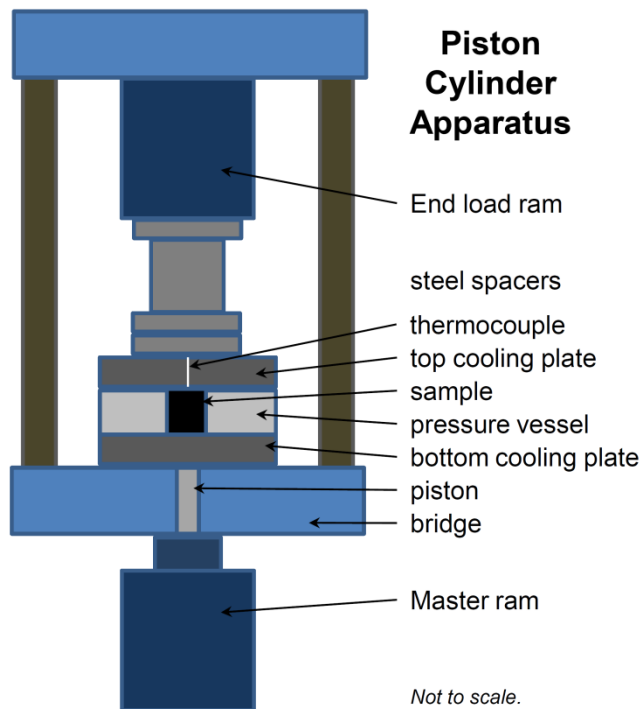


Figure 2.1. Sample assembly used for piston-cylinder experiments. Left, schematic of sample assembly. Right, photograph of components for the sample assembly (thermocouple not included). Not to scale.



Piston Cylinder Apparatus

- End load ram
- steel spacers
- thermocouple
- top cooling plate
- sample
- pressure vessel
- bottom cooling plate
- piston bridge
- Master ram

Not to scale.



Figure 2.2. Design of piston-cylinder apparatus. Left, schematic of piston-cylinder apparatus, based on the design of Boyd and England, 1960. Right, photograph of the piston-cylinder apparatus used for this study.

Table 2.1. Summary of samples and experimental conditions for olivine-diopside partitioning experiments.

Sample Name	Mineral Inputs^a	LiBaS #^b (Li source)	[Li]^b (ppm)	$\delta^7\text{Li}^c$ (‰)	Run Duration^d (days)	Temperature^d (°C)	Pressure^e (GPa)	Run Products^a
Li-31	ol, di, kspar, qtz	S1	100	+	1	1100	1.5	ol, di, quench
Li-30	ol, di, kspar, qtz	S1	100	+	3	1100	1.5	ol, di, quench
Li-27	ol, di, kspar, qtz	S1	100	+	5	1100	1.5	ol, di, quench
Li-42	ol, di, kspar, qtz	S3	100	0	1	900	1.5	ol, di, quench
Li-41	ol, di, kspar, qtz	S3	100	0	3	900	1.5	ol, di, quench
Li-43	ol, di, kspar, qtz	S3	100	0	5	900	1.5	ol, di, quench
Li-44	ol, di, kspar, qtz	S3	100	0	1	700	1.5	ol, di, quench
Li-39	ol, di, kspar, qtz	S3	100	0	3	700	1.5	ol, di, quench
Li-36	ol, di, kspar, qtz	S3	100	0	5	700	1.5	ol, di, quench
Li-37	ol, di, kspar, qtz	S3	100	0	10	700	1.5	ol, di, en, quench

^aol = olivine, di = diopside, kspar = orthoclase, qtz = quartz, en = enstatite, quench = glassy quench product and feathery orthopyroxene crystals

^bRefer to Section 2.2 for information regarding Li source.

^cLiBaS1 was made using an isotopically heavy stock solution, but $\delta^7\text{Li}$ was not measured.

^dThe 700 °C and 900 °C experiments were held at 1100°C for 1 day before being held at the temperature and duration listed.

^eRefers to the pressure felt on the sample.

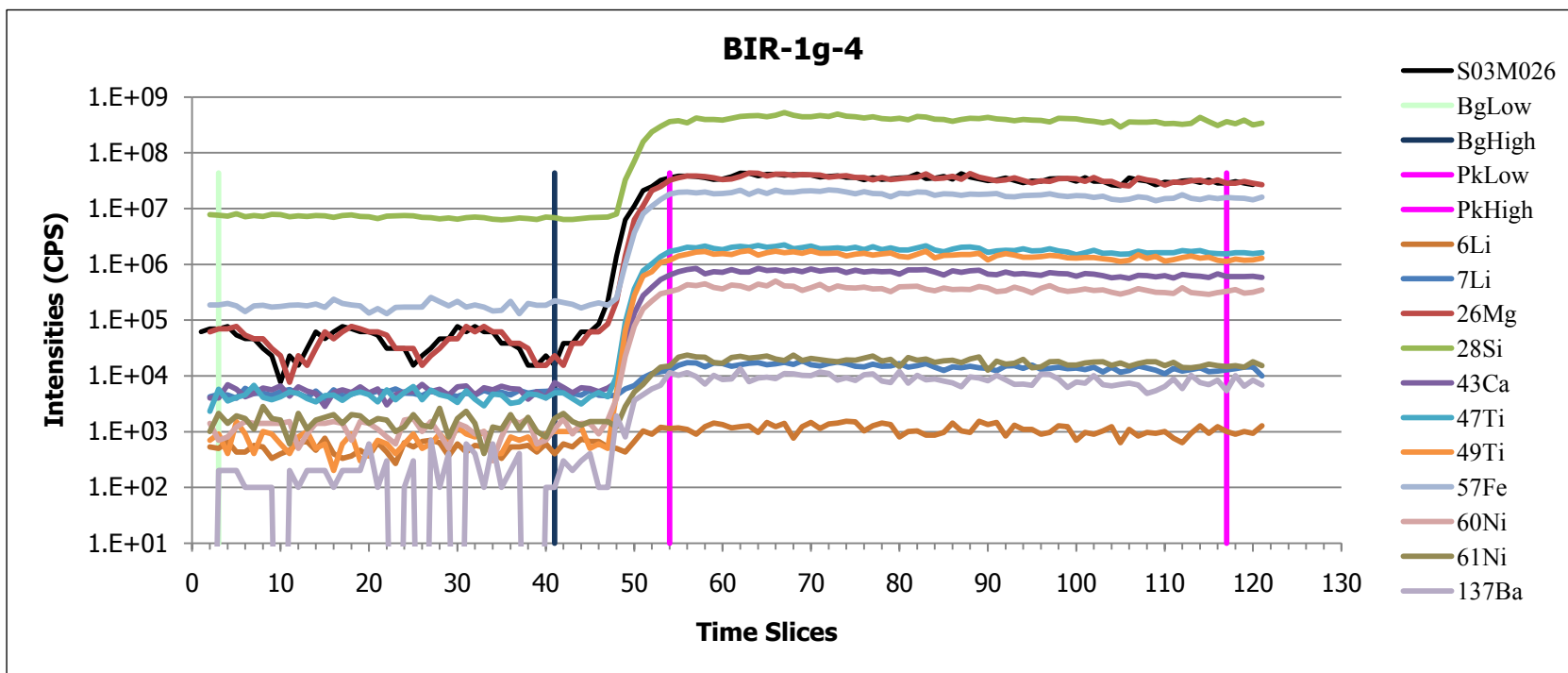


Figure 2.3. Example of a typical standard spectrum used for LA-ICP-MS sample-standard bracketing.

3 Results

3.1 Analytical Results

Backscattered images were acquired using the SEM for aliquots of all run products. Examples of images are presented in Figures 3.1-3.4. As can be seen from the images, the grains grew with sub- to euhedral shapes, and grew up to sizes of about 150 microns. Inclusions are apparent in many run product grains, most often of olivine inclusions within diopside grains, and were avoided during chemical analyses. Energy dispersive X-ray spectroscopy of run products confirms the presence of olivine, diopside, and enstatite, as well as quench products including orthopyroxene needles, and silica-rich glass spherules. Spectral patterns of olivines and diopsides showed occasional peaks for Fe and Cr, and Al, respectively. Spectral patterns of typical quench products show peaks for Si, O, Al, Ca, K, Ba, and occasionally Mg, Ti, Fe, or Cr.

Starting material and run product major element compositions for olivines and diopsides determined using EPMA are reported in Table 3.1. The FeO concentrations for run product grains are generally lower than 1 wt. % with the exception of olivine grains in two samples, Li-31 and Li-36. This is strikingly different from the starting material olivines, which have FeO averaging 9.11 wt. %. The FeO wt. % of the diopsides also drops between starting material and the run products, although this change is much less significant due to the very low FeO contents in the starting diopsides. The loss of iron from the system is attributed to the absorption of iron by the platinum capsule. As a response, the MgO wt. % must rise in the run product grains to account for the loss of iron. The variation in MgO wt. % for run product olivine grains ranged from 53.8-56.0, but there was virtually no variation in the run product diopside MgO wt. %. A more noticeable change between diopside starting materials and run products is the increase in Al₂O₃ wt. % and decrease in Na₂O wt. % for the run products. The increase in aluminum reflects the orthoclase component in solution. The decrease in Na₂O is attributed to its compatibility in fluid for the experimental conditions of this study.

Lithium concentrations for the starting materials and run products are presented in Table 3.2 and in Figure 3.5. The data show variable trends between Li concentration and

run duration for each temperature series (Figure 3.5). In general, run products from the 700 °C experiments contain about twice the amount of Li relative to those from the 900 °C and 1100 °C experiments. The 2σ error is much smaller for the 1100 °C experiments compared to the other temperatures; the 700 °C series shows the most variability in 2σ error (Table 3.2). The reported Ba concentrations (Table 3.2) for the run products are below detection limits in all but two experiments, and less than 7 ppm when detected.

3.2 Partition Coefficients

The partition coefficient, $D_{\text{Li}}^{(\text{ol/di})}$, is determined by dividing the average Li concentration in olivine by the average Li concentration in diopside within a given experiment. The calculated partition coefficients for Li between olivine and diopside for the experimental run products are listed in Table 3.3.

Lithium concentrations in olivine and diopside are plotted in Figure 3.6 for run products of the longer duration experiments. Visually, the partition coefficient can be approximated in Figure 3.6 as the slope of the trendline (forced through (0,0)), which is $D=2.3$, with an r^2 of 0.99. Figure 3.7 shows the $D_{\text{Li}}^{(\text{ol/di})}$ with respect to experimental temperature conditions. As can be seen in the figures, the partition coefficient remains constant for samples run at 700, 900, and 1100 °C. The average of the plotted partition coefficients is $2.2 (\pm 0.3)$.

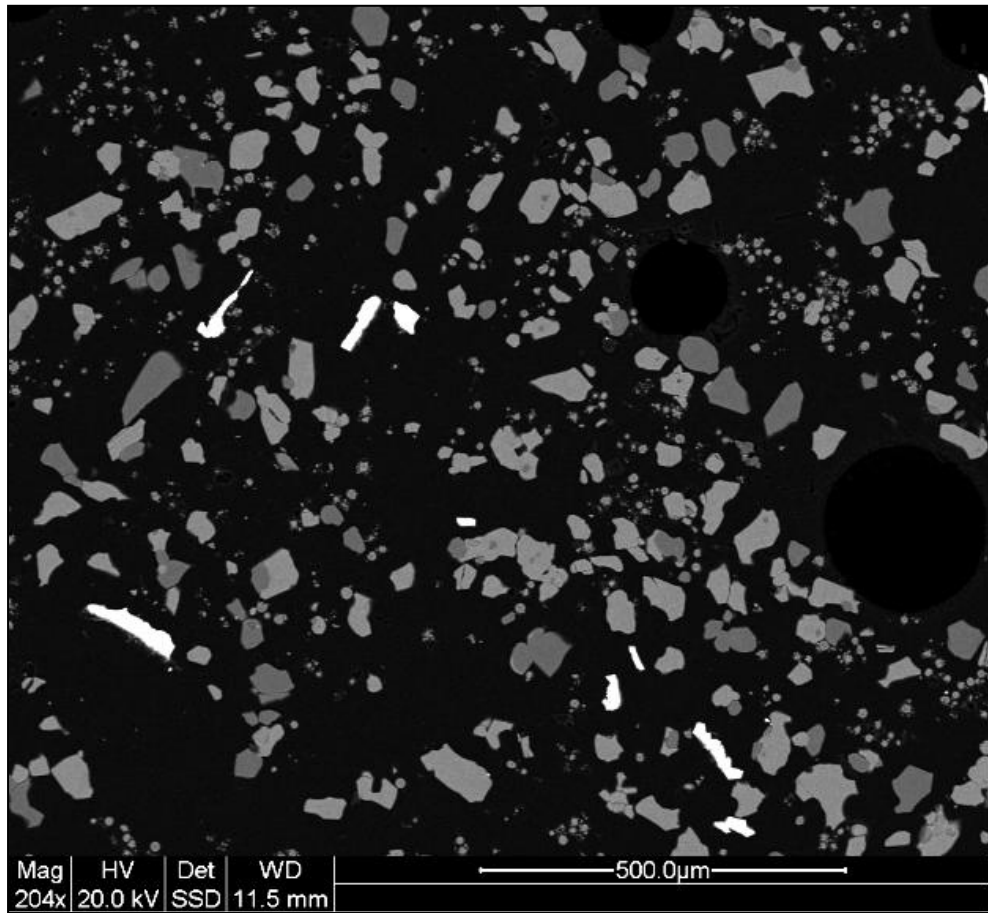


Figure 3.1. Backscattered SEM image of run product Li-27 (1100 °C, 5 days) grains mounted in epoxy. The brightest objects are remnants of the Ni crucible or Pt capsule that contained the charge. The darker gray grains are olivines and the lighter gray grains are diopsides. Smaller grains are quench products, consisting primarily of fused K-Al-silicate spherules.

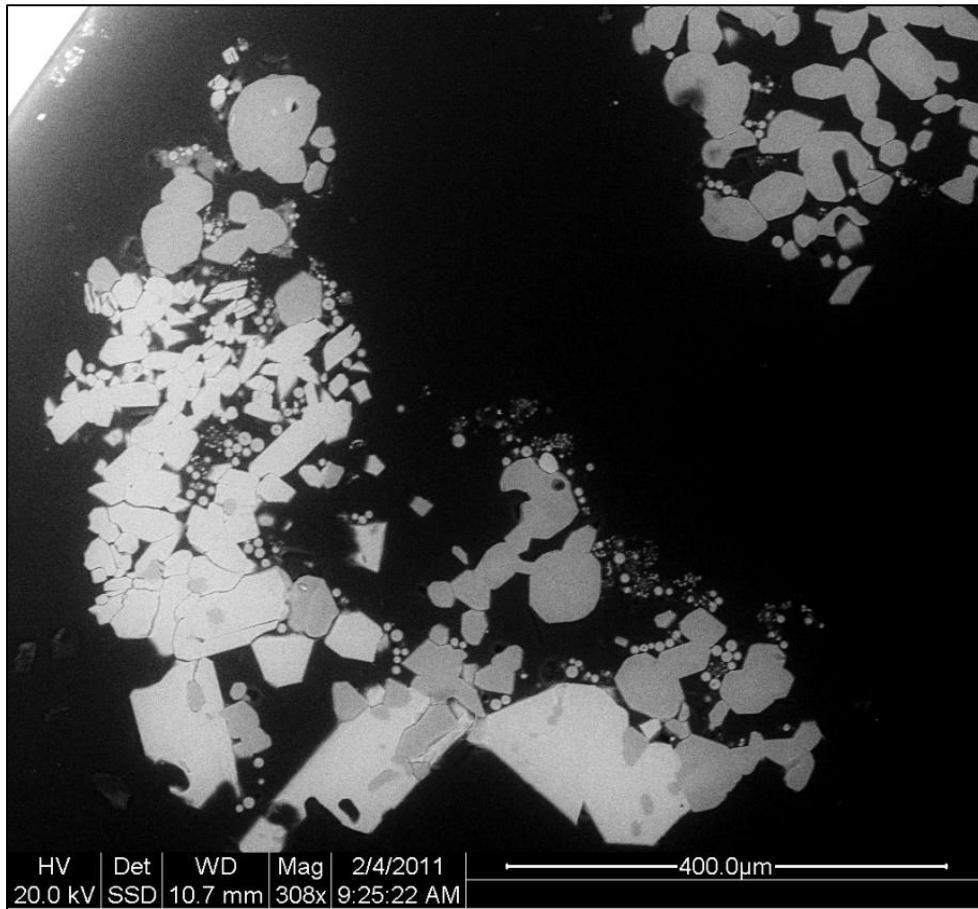


Figure 3.2. Backscattered SEM image of run product Li-43 (900 °C, 5 days) grains mounted in epoxy. The darker gray grains are olivines and the lighter gray grains are diopsides. Smaller grains are quench products.

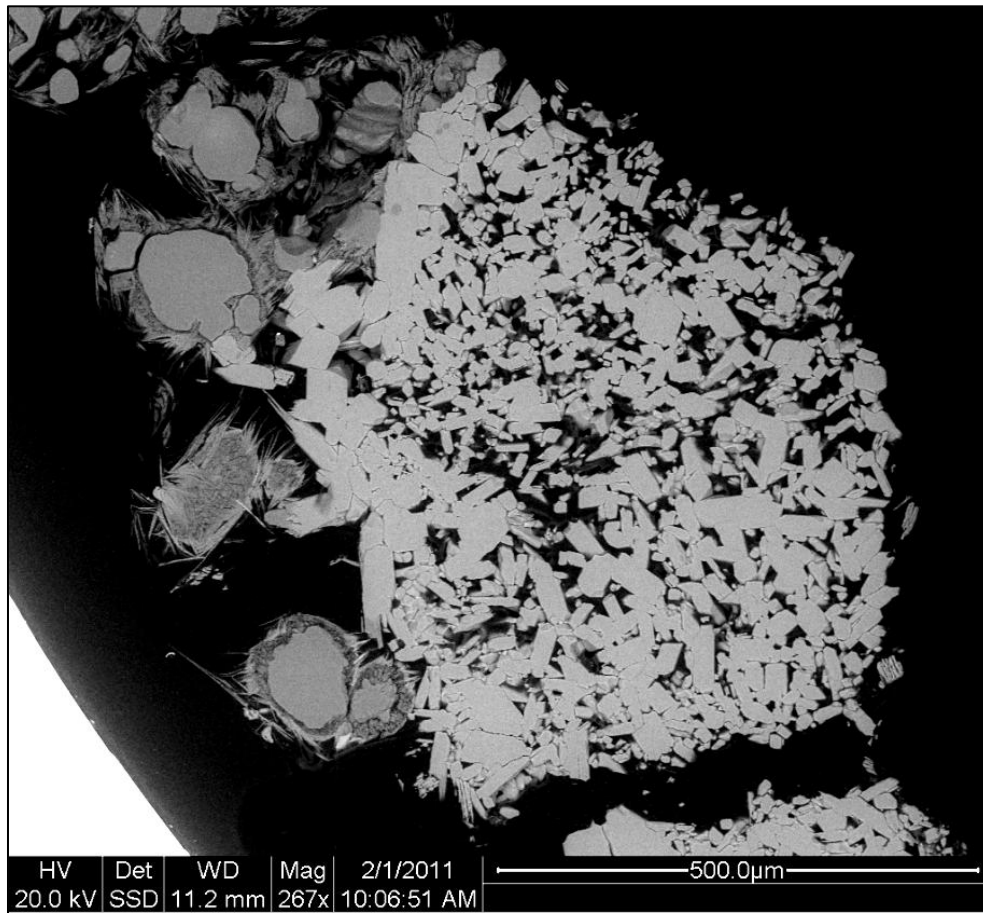


Figure 3.3. Backscattered SEM image of run product Li-39 (700 °C, 3 days) grains mounted in epoxy. The darker gray grains are olivines and the lighter gray grains are diopsides. Feathery crystals are quench products. The darker gray quench needles are primarily orthopyroxene, and the brighter quench needles are K-Al-silicates that rarely contain Ca and Ba.

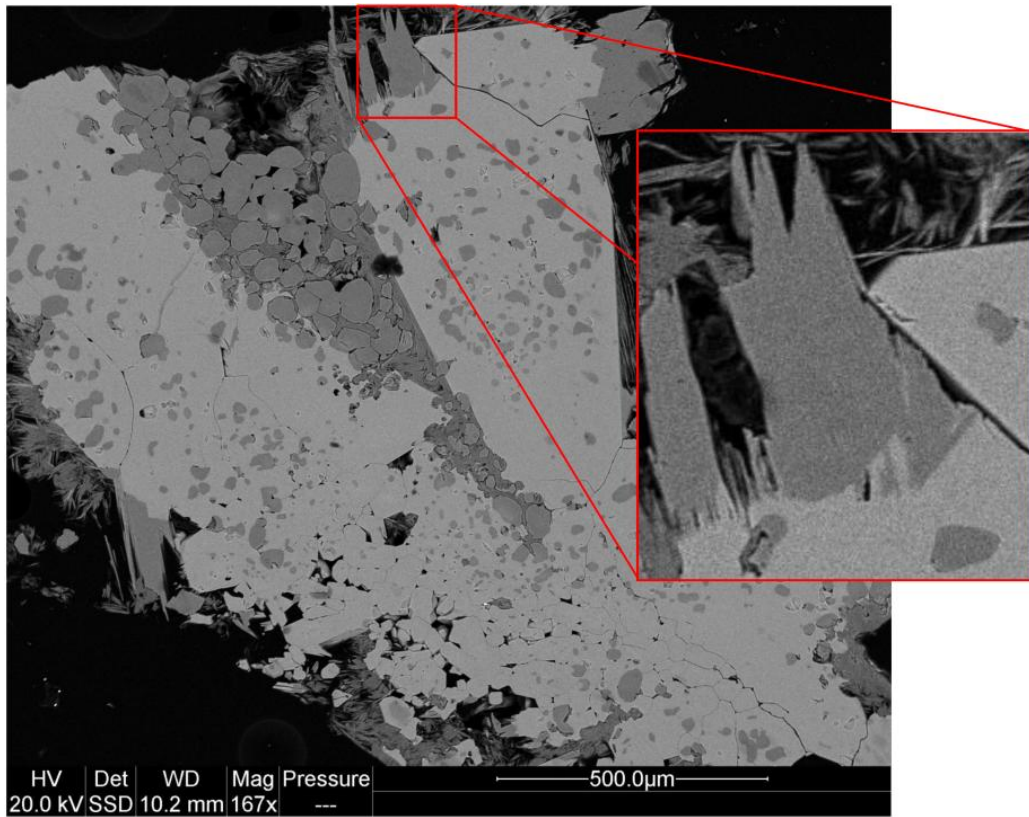


Figure 3.4. Backscattered SEM image of run product Li-37 (700 °C, 10 days) grains mounted in epoxy. The darker gray grains are either olivine or enstatite and the lighter gray grains are diopsides. Smaller grains are quench products, consisting primarily of feathery orthopyroxene needles. The box magnifies enstatite grain 1a.

Table 3.1. Major element concentrations of starting material and run product diopsides (DKD3, di), olivines (SCO2, ol), and enstatite (en) using EPMA (2 σ in parentheses).

Oxide or Element	n=14 DKD3	n=10 Li-31-di	n=6 Li-30-di	n=10 Li-27-di	n=20 Li-42-di	n=22 Li-41-di	n=18 Li-43-di	n=19 Li-44-di	n=22 Li-39-di	n=6 Li-36-di	n=19 Li-37-di
MgO	18.06 (0.54)	19.07 (0.58)	18.18 (0.42)	18.60 (0.64)	18.94 (0.54)	19.25 (0.88)	18.94 (0.50)	18.92 (0.46)	18.45 (1.16)	18.97 (1.46)	18.57 (0.74)
NiO	0.01 (0.02)	0.02 (0.02)	0.04 (0.06)	0.04 (0.12)	0.01 (0.02)	0.02 (0.02)	0.01 (0.02)	0.02 (0.02)	0.01 (0.02)	0.01 (0.02)	0.03 (0.04)
Al ₂ O ₃	0.54 (0.22)	1.16 (0.46)	1.51 (0.68)	1.20 (0.34)	1.46 (0.44)	1.65 (0.90)	1.36 (0.96)	1.07 (0.32)	0.84 (0.54)	1.39 (1.30)	1.25 (0.52)
Cr ₂ O ₃	0.01 (0.02)	0.06 (0.08)	0.10 (0.12)	0.08 (0.08)	0.05 (0.08)	0.06 (0.08)	0.05 (0.06)	0.07 (0.10)	0.04 (0.06)	0.01 (0.02)	0.08 (0.14)
SiO ₂	54.63 (1.02)	52.89 (0.84)	52.66 (1.22)	53.07 (1.16)	53.48 (0.94)	53.67 (1.14)	53.82 (0.94)	53.87 (0.76)	54.32 (1.10)	53.38 (1.32)	52.67 (0.98)
Na ₂ O	0.37 (0.16)	0.00 (0.02)	0.01 (0.02)	0.03 (0.06)	0.00 (0.02)	0.02 (0.04)	0.01 (0.02)	0.01 (0.02)	0.14 (0.36)	0.09 (0.28)	0.00 (0.00)
FeO ^a	0.89 (0.12)	0.29 (0.60)	0.29 (0.56)	0.29 (1.14)	0.13 (0.22)	0.32 (0.72)	0.14 (0.20)	0.22 (0.72)	0.54 (0.76)	0.44 (0.86)	0.46 (0.88)
TiO ₂	0.01 (0.02)	0.08 (0.14)	0.32 (0.48)	0.05 (0.08)	0.12 (0.12)	0.02 (0.02)	0.07 (0.10)	0.05 (0.10)	0.09 (0.20)	0.02 (0.00)	0.03 (0.04)
MnO	0.06 (0.04)	0.13 (0.14)	0.16 (0.12)	0.05 (0.04)	0.06 (0.06)	0.06 (0.06)	0.06 (0.08)	0.06 (0.04)	0.08 (0.06)	0.05 (0.04)	0.04 (0.02)
K ₂ O	0.01 (0.00)	0.01 (0.02)	0.00 (0.02)	0.02 (0.02)	0.01 (0.02)	0.01 (0.02)	0.00 (0.02)	0.00 (0.02)	0.00 (0.02)	0.01 (0.02)	NA
CaO	25.62 (0.54)	24.21 (0.30)	24.90 (0.28)	24.97 (0.68)	25.25 (0.38)	24.82 (0.46)	25.26 (0.46)	25.42 (0.38)	25.19 (0.40)	25.02 (0.42)	25.00 (0.38)
Total	100.20	97.92	98.18	98.39	99.51	99.89	99.72	99.70	99.69	99.39	98.13

Oxide or Element	n=17 SCO2	n=7 Li-31-ol	n=6 Li-30-ol	n=3 Li-27-ol	n=26 Li-42-ol	n=18 Li-41-ol	n=26 Li-43-ol	n=18 Li-44-ol	n=20 Li-39-ol	n=9 Li-36-ol	n=1 Li-37-ol	n=1 Li-37-en
MgO	49.67 (1.30)	53.84 (2.38)	54.22 (0.66)	55.33 (1.02)	55.66 (0.76)	55.66 (0.76)	55.85 (1.62)	55.53 (1.46)	56.01 (0.94)	55.53 (1.38)	54.28	38.17
NiO	0.37 (0.04)	0.13 (0.18)	0.04 (0.02)	0.03 (0.04)	0.07 (0.10)	0.06 (0.08)	0.18 (0.54)	0.05 (0.08)	0.06 (0.10)	0.12 (0.18)	0.04	0.06
Al ₂ O ₃	0.01 (0.02)	0.02 (0.02)	0.02 (0.02)	0.01 (0.02)	0.01 (0.02)	0.01 (0.02)	0.01 (0.02)	0.01 (0.02)	0.02 (0.02)	0.01 (0.02)	0.02	0.38
Cr ₂ O ₃	0.02 (0.04)	0.02 (0.04)	0.03 (0.04)	0.00 (0.00)	0.01 (0.02)	0.02 (0.04)	0.02 (0.04)	0.03 (0.06)	0.02 (0.04)	0.01 (0.02)	0.00	0.00
SiO ₂	41.08 (0.58)	42.03 (0.58)	42.19 (0.74)	41.96 (0.30)	42.53 (0.60)	42.59 (0.56)	42.37 (1.08)	42.69 (1.24)	42.74 (0.74)	43.00 (1.02)	42.68	58.48
Na ₂ O	0.00 (0.02)	0.01 (0.02)	0.01 (0.02)	0.03 (0.02)	0.00 (0.02)	0.00 (0.02)	0.01 (0.02)	0.00 (0.00)	0.00 (0.02)	0.00 (0.02)	0.00	0.00
FeO ^a	9.11 (1.74)	1.29 (3.58)	0.16 (0.18)	0.06 (0.02)	0.26 (0.48)	0.25 (0.56)	0.56 (1.06)	0.33 (0.32)	0.29 (0.40)	1.03 (1.40)	0.17	0.11
TiO ₂	0.00 (0.00)	0.00 (0.00)	0.02 (0.02)	0.01 (0.02)	0.01 (0.02)	0.01 (0.02)	0.00 (0.00)	0.00 (0.02)	0.01 (0.02)	0.00 (0.02)	0.01	0.00
MnO	0.13 (0.06)	0.27 (0.26)	0.80 (0.46)	0.12 (0.04)	0.20 (0.04)	0.12 (0.06)	0.18 (0.06)	0.16 (0.08)	0.38 (0.18)	0.14 (0.02)	0.21	0.32
K ₂ O	0.00 (0.00)	0.00 (0.00)	0.00 (0.00)	0.00 (0.00)	0.00 (0.00)	0.00 (0.00)	0.00 (0.00)	0.00 (0.00)	0.00 (0.00)	0.00 (0.00)	NA	NA
CaO	0.07 (0.04)	0.13 (0.02)	0.20 (0.06)	0.22 (0.00)	0.27 (0.30)	0.13 (0.06)	0.28 (0.62)	0.41 (0.50)	0.31 (0.28)	0.13 (0.04)	0.33	0.17
Total	100.46	97.72	97.69	97.76	99.02	98.85	99.45	99.22	99.85	99.98	97.74	97.7

^aAll iron reported as FeO.

All data collected at the University of Maryland using the JEOL JXA-8900 EPMA. See text for analytical methods. NA = Not analyzed.

Table 3.2. Trace element concentrations of starting material and run product diopsides (DKD, di), olivines (SCO, ol), and enstatite (en) using LA-ICP-MS (2σ in parentheses).

Sample	Temperature (°C)	Run Duration (days)	Mean [Li] (ppm)	Mean [Ba] (ppm)	n
<i>Starting Materials</i>					
DKD			6.4 (5.0)	BDL	5
DKD3			3.1 (0.6)	BDL	8
SCO			1.9 (0.6)	BDL	2
SCO2			1.7 (0.2)	BDL	3
<i>Standard as Unknown</i>					
BHVO ^a			3.3 (1.5)	91.3 (35.8)	33
<i>Diopside</i>					
Li-31-di	1100	1	16.9 (3.4)	BDL	3
Li-30-di	1100	3	6.9 (0.8)	BDL	2
Li-27-di	1100	5	7.9 (1.0)	BDL	3
Li-42-di	900	1	7.9 (5.0)	BDL	5
Li-41-di	900	3	4.7 (3.8)	BDL	5
Li-43-di	900	5	7.1 (4.6)	BDL	5
Li-44-di	700	1	7.8 (5.0)	BDL	5
Li-39-di	700	3	10.9 (4.2)	BDL	3
Li-36-di	700	5	13.4 (4.4)	1.7 (1.0)	6
Li-37-di	700	10	6.9 (1.8)	1.3 (0.6)	4
<i>Olivine</i>					
Li-31-ol	1100	1	21.2 (0.4)	BDL	3
Li-30-ol	1100	3	15.9 (3.6)	BDL	3
Li-27-ol	1100	5	17.8 (3.8)	BDL	3
Li-42-ol	900	1	14.4 (7.8)	BDL	5
Li-41-ol	900	3	9.7 (4.4)	BDL	5
Li-43-ol	900	5	14.6 (5.0)	BDL	5
Li-44-ol	700	1	22.1 (20.0)	BDL	5
Li-39-ol	700	3	32.3 (8.0)	BDL	4
Li-36-ol	700	5	30.4 (15.6)	BDL	6
Li-37-ol	700	10	16.1 (3.6)	BDL	5
<i>Enstatite</i>					
Li-37-en	700	10	59.9	6.8	1

^aBHVO standard was run as a sample with unknown concentration. Accepted concentrations for Li and Ba for BHVO are 4.6 ppm and 129.1 ppm, respectively (Potts *et al.*, 1992). The percent error is 28% for Li and 29% for Ba.

All data determined using the Thermo-Finnigan Element II ICP-MS with New Wave UP213 Laser Ablation system at the University of Maryland. BDL = Below detection limit.

Table 3.3. Partition coefficients ($D_{\text{Li}}^{(\text{ol/di})}$) for run products (2σ in parentheses). Italicized samples have not approached equilibrium.

Sample	Temperature (°C)	Run Duration (days)	$D_{\text{Li}}^{(\text{ol/di})}$
<i>Li-31</i>	1100	1	1.3 (0.2)
Li-30	1100	3	2.3 (0.6)
Li-27	1100	5	2.3 (0.6)
<i>Li-42</i>	900	1	1.8 (1.6)
Li-41	900	3	2.1 (2.0)
Li-43	900	5	2.2 (1.8)
<i>Li-44</i>	700	1	2.8 (3.2)
<i>Li-39</i>	700	3	3.0 (1.4)
Li-36	700	5	2.3 (1.4)
Li-37	700	10	2.4 (0.8)

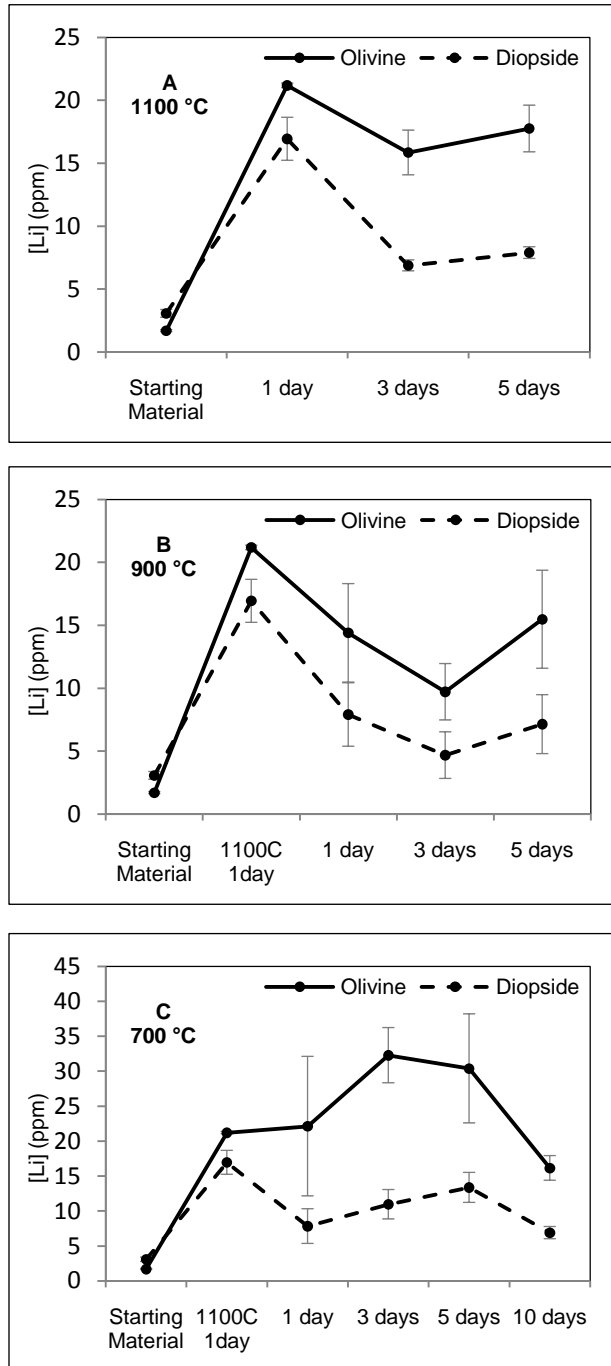


Figure 3.5. Li concentrations in olivine (solid line) and diopside (dashed line) for starting materials and the three temperature series investigated. A) Li concentrations for starting materials and 1100 °C experiments at 1, 3, and 5 days. B) Li concentrations for starting materials, 1100 °C 1 day treatment, and 900 °C experiments at 1, 3, and 5 days. C) Li concentrations for starting materials, 1100 °C 1 day treatment, and 700 °C experiments at 1, 3, 5, and 10 days.

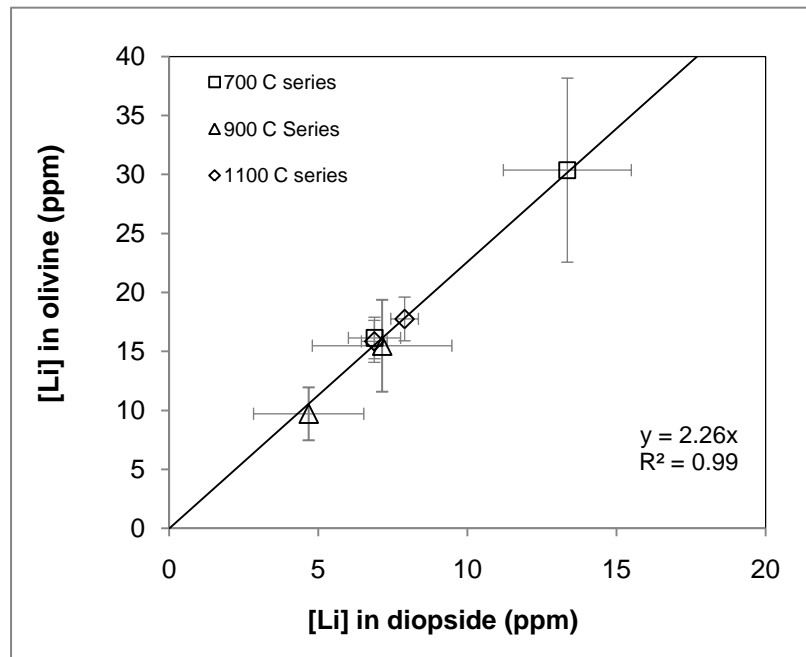


Figure 3.6. Lithium concentrations in olivine versus lithium concentrations in diopside for the run product grains that are interpreted to have approached equilibrium partitioning. Data are plotted for experiments lasting 5 and 10 days at 700 °C, 3 and 5 days at 900 °C, and 3 and 5 days at 1100 °C. The slope of the trendline indicates the partition coefficient ($D_{\text{Li}}^{\text{(ol/di)}}$) is ~ 2.3 for all temperature series investigated in this study.

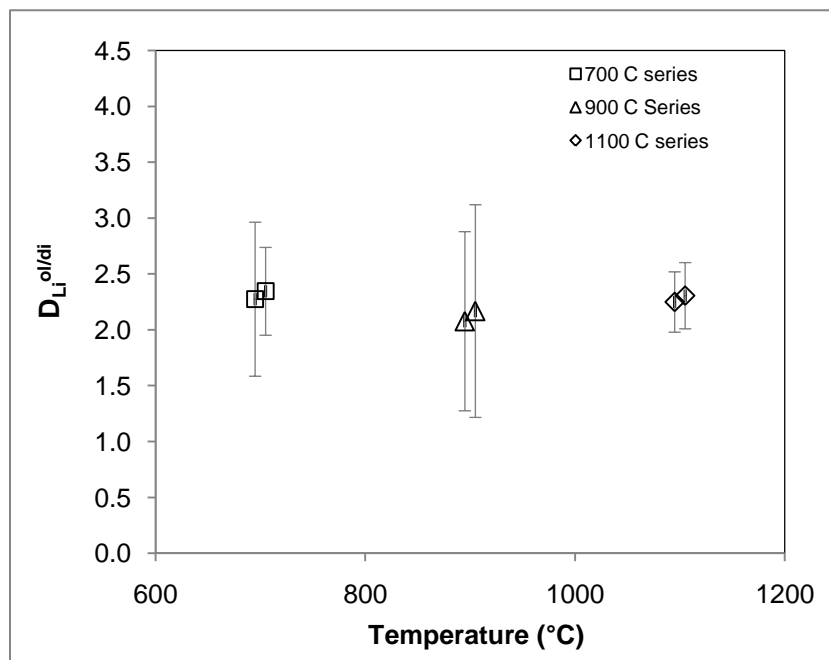


Figure 3.7. Measured partition coefficients ($D_{\text{Li}}^{\text{(ol/di)}}$) from experimental run products plotted versus temperature of experiment. Data are plotted for experiments lasting 5 and 10 days at 700 °C, 3 and 5 days at 900 °C, and 3 and 5 days at 1100 °C. Error bars represent 1σ deviations for each measured D . Values of measured $D_{\text{Li}}^{\text{(ol/di)}}$ for plotted experiments fall between 2 and 2.4, with an average of $2.2 (\pm 0.3)$.

4 Discussion

4.1 Assessment of Equilibrium

The goal of this study was to approximate equilibrium distributions of Li between olivine and diopside for three different temperatures relevant to upper mantle processes. Experiments were conducted at 700 °C, 900 °C, and 1100 °C for 1-10 days (Table 2.1). Approach to equilibrium can be assessed using a time series plot of the partition coefficients versus experiment duration for each temperature (Figure 4.1). For a given time series, equilibrium is considered to have been approached when the partition coefficient ceases to evolve as a function of time, which is observed as a flattening of the data trend. As Figure 4.1 shows for the 1100 °C series, the trend flattens after 3 days. Thus, the equilibrium partitioning of lithium for the 1100 °C series is approached by 3 days. Similarly, the 900 °C series approaches equilibrium Li partitioning by 3 days. The 700 °C experiments do not approach equilibrium conditions until 5 days. Because each 700 °C and 900 °C experiment endured a preliminary day at 1100 °C, I assume that at 0 days of the experiment for those temperatures, the partition coefficient equaled that of the 1 day, 1100 °C partition coefficient, 1.25. With this in mind, the partition coefficients for the 700 °C and 900 °C experiments indicate a marked redistribution of Li just one day after the temperature decrease from the preliminary day at 1100 °C, which is consistent with the fast diffusivity of Li.

The amount of Li incorporated into a crystal is dictated by a partition coefficient, and the diffusion rate of Li in the crystal controls the time needed for the equilibrium distribution of Li to be approached. As shown in Figure 4.1, the measured partition coefficients for olivine/diopside for the 700 °C series at 1 and 3 days have $D_{\text{Li}}^{(\text{ol/di})}$ values higher than the inferred equilibrium $D_{\text{Li}}^{(\text{ol/di})}$. The higher $D_{\text{Li}}^{(\text{ol/di})}$ for the 1 and 3 day experiments at 700 °C could be explained by faster diffusion in olivine, which gives the impression of an inflated olivine/diopside partition coefficient over a short timescale.

Low Ba concentrations for the run products (Table 3.2) indicate the absence of fluid inclusions and verify the incorporation of Li into the minerals themselves. The Li concentrations in olivine and diopside remain stable at 1100 °C after 3 days (Figure 3.4),

which supports the notion that equilibrium has been approached at that time for that temperature. The inferred equilibrium concentrations observed in the 900 °C series are within error of each other. The decrease in Li concentrations in both olivine and diopside in the 10 day 700 °C experiment may be explained by the presence of enstatite in the run products (Figures 3.4-3.5, Tables 3.1-3.2). The enstatite grains have high Li concentrations (~60 ppm), suggesting that small amounts of this phase could retain much of the Li in the system, making it less available to the olivine and diopside. Despite the variation in the trends of Li concentrations in olivine and diopside for the different run durations, the distribution of lithium between the two minerals remains constant for the durations approaching equilibrium.

Lithium isotopes were not measured for the present study, but the experimental design incorporated an isotopically controlled starting solution so that future workers would be able to measure Li isotope ratios for the run product grains. It should be noted that chemical equilibrium does not imply isotopic equilibrium. Chemical equilibrium entails a steady-state reaction, where there is constant exchange but no net removal or addition of chemical species. Isotopic equilibrium is not necessarily achieved at the same time that chemical equilibrium is established. For example, if ^6Li reacts more rapidly than ^7Li , this lighter isotope may be enriched in the product phase for some time even after the approach to chemical equilibrium has been made.

4.2 Trace Element Partitioning Theory and Mechanisms of Lithium Incorporation

Trace element partitioning is dependent upon the thermodynamic predictions of chemical equilibrium based on, among other things, chemical potentials, thermodynamic activities, and expressions for the Gibbs free energy (McIntire 1963). Goldschmidt (1937) presented a comprehensive review regarding the incorporation of elements into particular crystallographic sites, primarily based on ionic charge and radius. While exceptions to these rules may exist, they remain a solid foundation for the understanding of elemental incorporation into a crystal lattice.

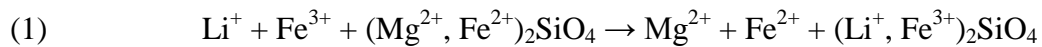
Many studies of trace element partitioning have focused on the partitioning of elements between solid phases and liquid phases, such as mineral precipitation from solution or crystallization from a melt. In most cases, trace element behavior is described by semi-empirical methods that fit measured partition coefficient data to models based on thermodynamic principles. The partition coefficient, sometimes referred to as the distribution coefficient (usually represented as D or K_D) is defined by the ratio of the concentration (C) of the element of interest (i) in one phase (A) to the concentration of that element in another phase (B): $D_i^{A/B} = [C_i]^A/[C_i]^B$. In order for the modeling of trace element behavior to be accurate, the values of the partition coefficients used in model equations must be equilibrium values, since the thermodynamic variables are based on equilibrium reactions.

Trace elements are useful for their passive nature; they themselves behave differently in response to differences in thermodynamic variables such as pressure, temperature, and composition, but they have no impact on the result of major thermodynamic processes (Blundy and Wood, 2003). Traditionally, the rare earth elements (REEs) have been at the forefront of geochemical tracers, but other elements have become important over time, including Ni, Sr, Rb, Fe, Mg, Co, Mo, Sc, Li, B, Be, and many others (Hart and Dunn, 1993; Beattie 1994; Green 1994; Ayers *et al.*, 1997; Brenan *et al.*, 1998a; Taura *et al.*, 1998; O'Neill and Eggins, 2002; Zanetti *et al.*, 2004; Filiberto *et al.*, 2009).

First addressed by Onuma *et al.* (1968), the dependence of the partition coefficient on the ionic radius follows a parabolic shape. Blundy and Wood (1994) refined the theory behind this observation, focusing on the elastic strain a lattice experiences when ionic radius varies for a particular site. For this study, the lattice strain model may be appropriate when considering Li incorporation into diopside, as coupled substitution of the pair Li^+ and Al^{3+} (or Fe^{3+}) may replace Ca^{2+} and Mg^{2+} . The incorporation of Li into the olivine structure, however, is likely to be in the Mg site because of their similar radii (0.76 Å for Li vs. 0.72 Å for Mg in octahedral coordination; Shannon, 1976). In this instance, the charge difference becomes more important than ionic radius. Wood and Blundy (2001) investigated the effects of charge on trace

element partitioning and found that there is an approximately parabolic dependence of the partition coefficient on charge. In each study, the partition coefficient can be predicted based on the model for a given set of temperature, pressure, and composition parameters. This method of deducing partition coefficients serves as a useful check for experimentally observed partition coefficients.

Lithium has a charge of 1^+ and an ionic radius of 0.76 \AA for an octahedrally coordinated lattice site (Shannon 1976). These characteristics make lithium suitable for incorporation into the olivine and diopside crystal structures in one of three places: an interstitial site, a vacant octahedral site, or an occupied octahedral site (Dohmen *et al.*, 2010). Because of its size, a lithium ion can readily substitute for an octahedrally coordinated Mg^{2+} ion, which has an ionic radius of 0.720 \AA (Shannon 1976). However, a charge balancing reaction is necessary if Li is to substitute for Mg. Using olivine as an example, Li is a suitable monovalent cation for the M1 or M2 sites, but necessitates the incorporation of a trivalent cation to satisfy charge balance (Suzuki and Akogi, 1995). One mechanism for charge balancing could be a coupled substitution with ferric iron according to the equation:



This exchange mechanism is plausible provided that the oxygen fugacity ($f\text{O}_2$) is sufficiently high to support significant Fe^{3+} . In her experiments of lithium partitioning between olivine and clinopyroxene, Caciagli-Warman (2010) showed that having a $\log f\text{O}_2$ of -15 at $1000 \text{ }^\circ\text{C}$ generated $D_{\text{Li}}^{(\text{ol}/\text{cpx})}$ of 0.7, whereas a higher $\log f\text{O}_2$ of -10.3 at $1000 \text{ }^\circ\text{C}$ generated $D_{\text{Li}}^{(\text{ol}/\text{cpx})}$ of 4.0. The experiments in this study were unbuffered with respect to oxygen fugacity, and no effort was made to measure the within-run $f\text{O}_2$ directly. Previous experiments conducted using essentially the same assembly and bulk composition (De Kalb diopside and water) found $f\text{O}_2 \approx -11.5$ in unbuffered experiments at $900 \text{ }^\circ\text{C}$ and 20 kb (Brenan *et al.*, 1995a), suggesting that sufficient Fe^{3+} should be available. A similar coupled substitution is expected for Li substitution in the diopside, although Al^{3+} is likely to be the preferred species for coupled substitution based on the measured Al contents in run product diopsides. Other possible trivalent species for

coupled substitution in olivine and diopside include Cr^{3+} , Sc^{3+} , V^{3+} , and REE^{3+} (Seitz and Woodland, 2000).

4.3 Comparison to Other Studies of Lithium Partitioning

High temperature (900 – 1200 °C) experiments at 1 atm were conducted by Coogan *et al.* (2005) from 2 to 50 hours in order to determine the temperature-dependence of the partition coefficient for Li between plagioclase and clinopyroxene. Their results showed a strong temperature-dependence of the partition coefficient, with $\ln(D_{\text{Li}}^{\text{(plag/cpx)}})$ decreasing from 1200 to 900 °C. The temperature-dependence of $D_{\text{Li}}^{\text{(plag/cpx)}}$ shown by Coogan *et al.* (2005) indicates that during cooling there can be diffusive redistribution of Li from plagioclase into clinopyroxene.

The partition coefficients for Li between olivine and diopside determined in this study fall within the range of partition coefficients reported in other studies. Figure 4.2 shows the Li concentrations in olivine vs. the Li concentrations in clinopyroxenes for this and other published studies. Data from this study fall very nicely along the 2.2:1 trendline that runs through the published values for other experimental studies and for natural mantle xenolith samples. The largest scatter exists among the natural mantle xenolith samples, which likely reflects disequilibrium in dynamic natural systems. It should be noted that all points from experimental studies (with the exception of three from the aqueous solution study by Caciagli-Warman, 2010, bolded diamonds) on Figure 4.2 were plotted using data from olivine-only or diopside-only experiments; minerals from experiments run at similar P-T conditions were used to create olivine-diopside partition coefficients.

Experiments to determine Li partitioning between olivine/melt and clinopyroxene/melt were conducted by Brenan *et al.* (1998a) at 1-1.5 GPa and 1000 to 1350 °C. Only one experiment contained both olivine and clinopyroxene, for which the concentrations of Li in each mineral were reported to be identical, producing a $D_{\text{Li}}^{\text{(ol/cpx)}}$ of 1. For two experiments where olivine and clinopyroxene were run separately but with similar P-T conditions, the calculated olivine/cpx Li partition coefficient was 0.53. The authors suggest that mineral/melt partitioning of Li varies as a function of mineral and

melt composition. Blundy and Dalton (2000) investigated trace element partitioning between minerals and carbonate melt. For three of their experiments, a partition coefficient for Li between olivine and clinopyroxene could be calculated ($D_{\text{Li}}^{\text{(ol/cpx)}} = 0.70, 0.75, 0.99$). Blundy and Dalton (2000) attribute differences in mineral/melt partitioning between carbonate and silicate melts to differences in melt structures. The partition coefficients found by both Brenan *et al.* (1998a) and Blundy and Dalton (2000) favor Li incorporation into clinopyroxene, which disagrees with the results of this study.

A recent PhD Thesis (Caciagli-Warman 2010) conducted at the University of Toronto investigated the partitioning of Li between olivine/fluid and clinopyroxene/fluid at 800-1200 °C and 1 GPa. In that study, most experiments investigated the olivine/ and diopside/fluid partitioning in separate runs, although two samples contained both olivine and diopside in the same experiment (Caciagli-Warman 2010). Her study and this study both came to the same conclusion, that the partition coefficient for lithium between olivine and diopside is not temperature dependent over the range of pressures and temperatures investigated. Caciagli-Warman further showed that an increase in oxygen fugacity causes an increase in the Li partition coefficient between olivine and diopside. An increase in oxygen fugacity would cause an increase in Fe^{3+} relative to Fe^{2+} , which could potentially charge balance more Li^+ substituting into the Mg octahedral site in olivine, thus causing an increase in $D_{\text{Li}}^{\text{(ol/di)}}$.

4.4 Implications for Observed $\delta^7\text{Li}$ in Mantle Xenoliths

Analysis of $\delta^7\text{Li}$ in mineral separates and *in situ* analysis of individual phases from mantle xenoliths from diverse localities have revealed that olivines and pyroxenes from a single sample are commonly characterized by different isotope ratios, most commonly with lighter Li measured in the pyroxenes (Seitz *et al.*, 2004; Jeffcoate *et al.*, 2007; Rudnick and Ionov, 2007; Ionov and Seitz, 2008). There are three conceivable models that could explain the observation of lighter Li in clinopyroxene relative to the olivine: 1) the isotopic fractionation factor ($\alpha_{\text{Li}}^{\text{ol-cpx}}$) is > 1 at high temperatures; 2) the olivine-clinopyroxene partition coefficient is temperature-dependent over a range relevant to mantle xenolith exhumation; 3) differing rates of Li diffusion from an

infiltrating melt or fluid are preserved in olivine and clinopyroxene. Each of these models will be addressed in turn.

1) Isotopic Fractionation Factor > 1 at High Temperatures

In this model, the isotopic fractionation factor for lithium between olivine and clinopyroxene ($\alpha_{\text{Li}}^{\text{ol-cpx}}$) in mantle xenoliths would be > 1 at higher temperatures (~1000 °C). The fractionation factor, defined as $\{^7\text{Li}/^6\text{Li}\}_{\text{ol}}/\{^7\text{Li}/^6\text{Li}\}_{\text{cpx}}$, is generally expected to equal 1 at such high temperatures since the fractionation of stable isotopes is diminished as temperature increases (Northrop and Clayton, 1966; Criss and Farquhar, 2008). If $\delta^7\text{Li}$ is lighter in clinopyroxene, which is observed for many natural xenolith samples (Seitz *et al.*, 2004; Jeffcoate *et al.*, 2007; Rudnick and Ionov, 2007; Ionov and Seitz, 2008), then $\alpha_{\text{Li}}^{\text{ol-cpx}}$ would have to be greater than one if the olivine and clinopyroxene were in isotopic equilibrium. In order to assess Li isotope fractionation at higher temperatures, Tomascak *et al.* (1999a) studied samples from Kilauea Iki Lava Lake, which is the product of a single eruptive event and an example of closed system basaltic differentiation by fractional crystallization of olivine + clinopyroxene \pm plagioclase \pm oxides. Despite a large degree of fractional crystallization for the lavas sampled, Tomascak *et al.* (1999a) observe no per mil-level Li isotope fractionation occurring during magmatic differentiation at > 1050 °C. In light of the results presented by Tomascak *et al.* (1999a), the first model explaining lighter Li in clinopyroxene (relative to olivine) from mantle xenoliths is unlikely.

2) Temperature-Dependent Partition Coefficient

In this model, the partition coefficient of Li between olivine and clinopyroxene decreases with temperature, causing Li to diffuse from olivine to clinopyroxene upon cooling. Because ^6Li diffuses faster than ^7Li (Richter *et al.*, 2003), clinopyroxene would receive lighter Li more quickly than it receives the heavier. Ionov and Seitz (2008) argue that eruption style (and therefore cooling duration) is the most important factor controlling observed lighter $\delta^7\text{Li}$ in clinopyroxene. In particular, they suggest that lava-hosted xenoliths endure longer cooling periods and therefore have more opportunity to undergo redistribution of Li as a function of the temperature-dependent partition

coefficient. As Coogan *et al.* (2005) have shown a strong temperature-dependence of Li partitioning between clinopyroxene and plagioclase, Ionov and Seitz (2008) suggest the possibility of other mineral pairs having a temperature-dependent D_{Li} , which could offer explanations for unexpected Li elemental and isotopic trends observed in natural samples.

Gallagher and Elliott (2009) developed a numerical model for Li isotopic diffusion using temperature-dependent diffusivity and partitioning parameters between crystals and melts, with the intent to see if diffusion driven by the natural cooling of lavas could adequately explain Li isotopic fractionation trends observed for natural xenolith samples. Their modeling shows using temperature-dependent diffusivities and partition coefficients that natural cooling can cause the isotopic fractionation trends observed in natural xenolith phenocrysts for the temperature range 750 °C to 1200 °C. The model for which the partition coefficient is held constant shows that temperature-dependent diffusivity alone can have substantial effects on the Li isotopic composition. For olivine and diopside separates over this temperature range, temperature-dependence of partition coefficients is therefore not required for the generation of Li isotopic variability. Gallagher and Elliott (2009) call for improved physical parameters, particularly regarding the temperature-dependence of the partition coefficient between various phases.

This thesis has demonstrated a lack of temperature-dependence of $D_{Li}^{(ol/di)}$ at equilibrium conditions over the temperature range 700 °C to 1100 °C. Since the partition coefficient is constant, there is no diffusive redistribution of lithium between olivine and diopside that would generate a disequilibrium isotopic ratio as a result of cooling alone.

3) Differing Li Diffusion Rates in Olivine and Clinopyroxene

In the third model, Li would diffuse into olivine and clinopyroxene at different rates from an infiltrating melt or fluid. This external source provides new Li to the system and can generate the observed light δ^7Li in clinopyroxenes with faster clinopyroxene diffusion rates, because 6Li diffuses faster than 7Li (Richter *et al.*, 2003). Figure 1.2 presents a summary of the published δ^7Li values for olivines and pyroxenes from mantle xenoliths. Peridotite xenoliths from Arizona, Siberia, Austria, and Germany all show δ^7Li higher in olivine relative to clinopyroxene; the most extreme fractionation

observed for one of the German samples is $\delta^7\text{Li}_{\text{ol}} = 1.4$, $\delta^7\text{Li}_{\text{cpx}} = -2.4$ ($\Delta^7\text{Li}_{\text{ol-cpx}} = 3$) (Seitz *et al.*, 2004). The olivine-clinopyroxene partition coefficients reported in that study range from 0.93 to 1.83 for the various peridotite xenolith samples investigated; the $\delta^7\text{Li}$ values for those same samples always showed heavier Li in olivines ($\delta^7\text{Li} = 1.4$ to 4.5) and lighter Li in clinopyroxenes ($\delta^7\text{Li} = -2.4$ to 3.0). The comparison of the equilibrium partition coefficient for Li between olivine and diopside from this study (2.2) and the partition coefficients from Seitz *et al.* (2004) suggest that the crystals sampled by Seitz *et al.* (2004) represent non-equilibrium conditions.

Jeffcoate *et al.* (2007) investigated Li abundances and isotopic ratios in olivines and clinopyroxenes from peridotites and mafic melts. Their measurements generally show that olivines retain close to twice as much Li as the clinopyroxenes, which agrees with the findings of this study and implies that the xenoliths from the Jeffcoate *et al.* (2007) study are chemically equilibrated. However, Jeffcoate *et al.* (2007) report isotopic compositions of mineral separates from the xenoliths from Siberia and Mongolia that show significant variation of $\delta^7\text{Li}$ in clinopyroxene ($\delta^7\text{Li} = -8.7$ to 6.6 ‰) compared to olivine ($\delta^7\text{Li} = 3.0$ to 5.2‰). Additionally, they report isotopic variations between phases; eight out of the ten measured xenolith samples had heavier $\delta^7\text{Li}$ for olivines relative to clinopyroxenes. The authors explain the observed isotopic disequilibrium by suggesting diffusive transfer of Li from interstitial melt veins prior to continued isotope fractionation due to solid-state diffusion in minerals. A transect of an olivine grain from the San Carlos xenolith shows a heavier $\delta^7\text{Li}$ rim (Jeffcoate *et al.*, 2007), which could indicate diffusive movement of lighter Li out of the olivine into another phase. Jeffcoate *et al.* (2007) claim that the isotopic disequilibrium observed in their samples occurred during the late stage magmatism that transported the xenoliths, if not the final cooling itself. Based on the results of this thesis, bulk transfer of Li is not expected between olivine and diopside as a result of cooling. Thus, addition of Li during the magmatic event would be the preferred explanation.

Rudnick and Ionov (2007) investigated Li elemental and isotopic disequilibrium for olivines and pyroxenes from Russian Tok peridotite xenoliths. Most of the samples from their study do not correspond with the range of equilibrium partitioning predicted

by previous work, $D_{\text{Li}}^{(\text{ol}/\text{cpX})} = 1.1$ to 2.0 (Brenan *et al.*, 1998a; Eggins *et al.*, 1998; Seitz and Woodland, 2000), or that determined in this study (2.2). Rudnick and Ionov (2007) report $\delta^7\text{Li}$ in olivine ranging from -2 to 12‰, and $\delta^7\text{Li}$ in clinopyroxene ranging from -1 to -15 ‰, with $\delta^7\text{Li}$ consistently lower for clinopyroxenes than olivines. Rudnick and Ionov (2007) suggest as an explanation the recent addition of Li to the Tok peridotites from an infiltrating grain boundary fluid or melt, producing Li zonation and resulting in diffusion-driven kinetic isotopic fractionation due to differences in Li diffusion rates for olivine and clinopyroxene.

Published studies regarding diffusion of Li in olivines and clinopyroxenes at high temperatures are very limited. An experimental study of Li diffusion in clinopyroxene over the temperature range 800 to 1100 °C by Coogan *et al.* (2005) found the Li diffusion coefficient for clinopyroxene to be $5.0\text{E-}15 \text{ m}^2\text{s}^{-1}$ for 800 °C, $2.5\text{E-}13 \text{ m}^2\text{s}^{-1}$ for 900 °C, and $3.9\text{E-}13 \text{ m}^2\text{s}^{-1}$ for 1100 °C. A model developed by Dohmen *et al.* (2010), based on observations of high temperature experiments, generates Li diffusion coefficients for two mechanisms of incorporation for olivine: an interstitial site and an octahedrally coordinated metal site. The Li diffusivities of the interstitial site and octahedral site are, respectively, $2.1\text{E-}13 \text{ m}^2\text{s}^{-1}$ and $4.0\text{E-}17 \text{ m}^2\text{s}^{-1}$ for 798 °C, $4.2\text{E-}12 \text{ m}^2\text{s}^{-1}$ and $1.0\text{E-}15 \text{ m}^2\text{s}^{-1}$ for 997 °C, and $2.0\text{E-}10 \text{ m}^2\text{s}^{-1}$ and $5.5\text{E-}14 \text{ m}^2\text{s}^{-1}$ for 1200 °C. Activation energies reported for the interstitial and octahedral sites are 220 and 240 kJ/mol, respectively (Dohmen *et al.*, 2010). Depending on which mechanism holds more control on Li diffusion in olivine, Li diffusion in clinopyroxene could be faster or slower than Li diffusion in olivine (Figure 4.3). However, the authors propose that the slow mechanism (octahedrally-coordinated metal site) is expected to control Li diffusion in olivines. If the Dohmen *et al.* (2010) model is accurate, it signifies that Li diffuses up to two orders of magnitude faster in clinopyroxene than in olivine. Figure 4.3 is an Arrhenius plot showing these data. Assuming these Li diffusion rates for olivine (octahedrally-coordinated metal site) and clinopyroxene are correct, the observed Li isotopic distribution in natural samples can be explained by the faster diffusion of Li into clinopyroxene from an infiltrating melt or fluid, with ^6Li diffusing faster than ^7Li . More Li diffusion experiments for olivine and clinopyroxene are needed to constrain these observations.

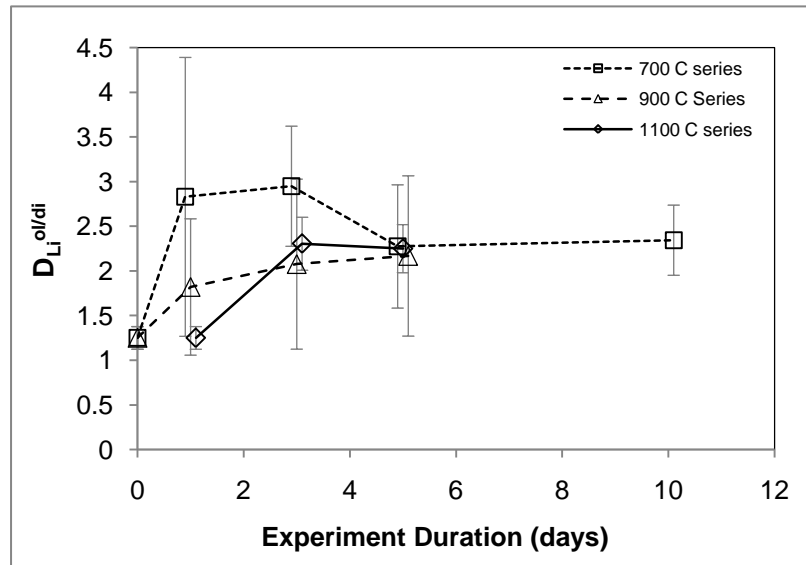


Figure 4.1. Measured partition coefficients ($D_{Li}^{ol/di}$) are plotted against experiment duration (days). Error bars are 1σ deviations. As the 700 °C and 900 °C series each endured a preliminary day at 1100 °C (for enhanced grain growth), at zero days the 700 °C and 900 °C series are assumed to have a partition coefficient equal to that observed for the 1 day, 1100 °C experiment. The 1100 °C series and 900 °C series are interpreted to approach equilibrium after three days and the 700 °C series is interpreted to approach equilibrium after five days.

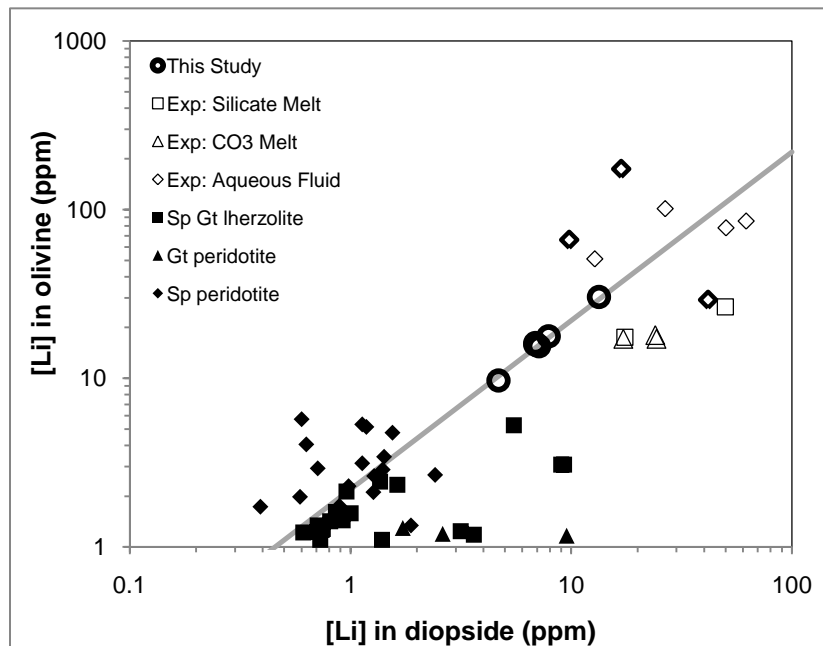


Figure 4.2. Plot comparing Li concentrations in olivine and diopside found in this study to published data. Open circles are data from this study, open diamonds are experimental studies with aqueous fluid, bold open diamonds showing experiments containing both olivine and diopside (Caciagli-Warman, 2010), open triangles are experimental studies with carbonate melt (Blundy and Dalton, 2000), and open squares are experimental studies with silicate melt (Brenan *et al.*, 1998a), and filled circles are natural mantle xenolith samples (Seitz and Woodland, 2000; Paquin and Altherr, 2002; Woodland *et al.*, 2004). The data tend to fall on a linear 2.2:1 trendline (gray line) with some of the mantle xenolith samples deviating significantly.

Sp = spinel, Gt = garnet.

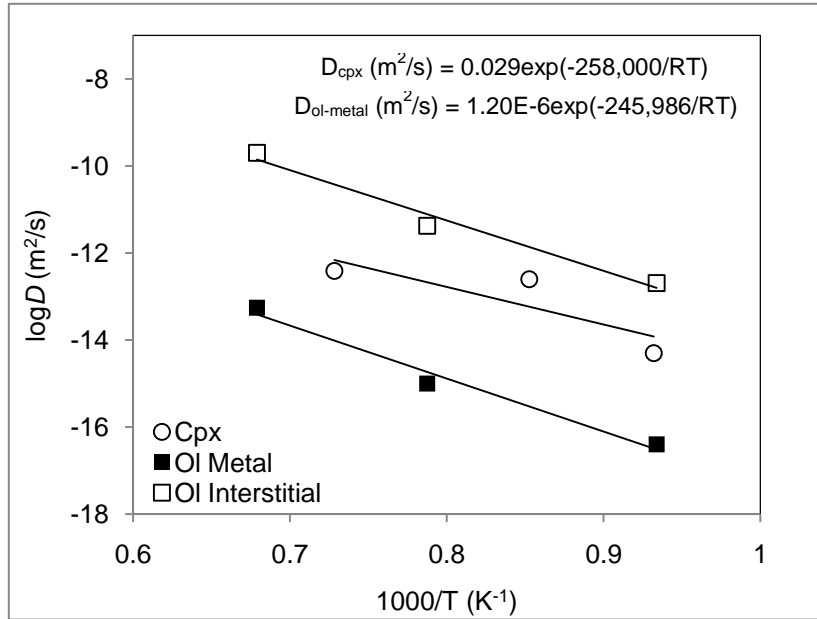


Figure 4.3. Arrhenius plot of Li diffusion coefficients measured for clinopyroxene (Coogan *et al.*, 2005) and olivine (Dohmen *et al.*, 2010). Two diffusion mechanisms for Li diffusion in olivine are plotted (interstitial site and octahedrally-coordinated metal site). The metal site is expected to control Li diffusion in olivine. The data show that Li diffuses faster in clinopyroxene (by one or two orders of magnitude) than metal site Li diffusion in olivine.

5 Conclusions

This study presents data for lithium partitioning between olivine and diopside at 1.5 GPa and 700 °C, 900 °C, and 1100 °C. Measured partition coefficients for experiments that are inferred to have approached equilibrium reveal $D_{\text{Li}}^{(\text{ol/di})} = 2.2 (\pm 0.3)$, with no dependence on temperature over the studied range. Thus, temperature-dependence of $D_{\text{Li}}^{(\text{ol/di})}$, which would lead to diffusive re-equilibration of Li between the two phases during eruption and cooling, is not an acceptable explanation for the observation of different $\delta^7\text{Li}$ values for olivines and clinopyroxenes frequently observed in mantle xenoliths.

Assuming that the temperature dependence of the partition coefficient is no longer a sufficient explanation for observed isotopic disequilibria, the two possible remaining explanations are an isotopic fractionation factor > 1 at higher temperatures, or diffusion of lithium at different rates from a fluid or melt. Results from Tomascak *et al.* (1999a) on Li isotopes from Kilauea Iki Lava Lake suggest that the fractionation factor equals one at temperatures above 1050 °C. If this result is interpreted to hold for mantle xenoliths, the observed light $\delta^7\text{Li}$ in clinopyroxenes cannot be best explained by equilibrium fractionation.

The next step for future research is to analyze the run products from these experiments for Li isotope ratios in order to determine the equilibrium isotope fractionation factor (α) and verify the results of Tomascak *et al.* (1999a). The experiments conducted for this study were done using a solution with a controlled Li isotopic composition. Therefore, the run products from this experiment can be analyzed for Li isotope ratios and the variation, if any, can be quantified. Also, an investigation of Li diffusion rates in olivines and diopsides at mantle temperature and pressure conditions would provide a useful constraint for researchers wishing to model the interactions of mantle xenoliths with an external Li source, such as a fluid or melt.

6 Failed Carbonate Experiments: Lessons Learned

6.1 Motivation

The initial experimental design for determining the equilibrium Li partition coefficient between olivine and diopside involved using carbonate powder as a lithium source to natural olivine ($[\text{Mg}_{1.8}, \text{Fe}_{0.2}]\text{SiO}_4$, San Carlos, Arizona) and diopside ($\text{CaMgSi}_2\text{O}_6$, De Kalb Junction, New York) grains (~100-150 microns). Lithium carbonate powder was chosen as the Li flux for the high-pressure, high-temperature experiments because an HCl rinse would separate the residual flux from the mineral grains for analysis. Recovered run products were analyzed using multi-collector inductively coupled plasma mass spectrometry for Li concentrations and isotope ratios. Experiments containing both olivine and diopside were analyzed by laser ablation inductively coupled plasma mass spectrometry and secondary ion mass spectrometry.

6.2 Methods

Sample Preparation and Piston Cylinder Experiments

A mixture of BaCO_3 and Li_2CO_3 powders (“LiBaC”) was prepared with a particular Li concentration and isotopic composition to serve as the Li source for the experiment with barium serving as a check (see Table 6.1 for LiBaC concentrations). Barium is incompatible in olivine or diopside, so the presence of Ba in significant amounts (> 15 ppm) would indicate contamination by the source powder such that Li measurements may not represent incorporation of Li into the mineral structure. The LiBaC powder was thoroughly mixed with 150 μm -sized olivines and/or diopsides using a Turbula mixer to satisfy the ratio of 2:1 LiBaC:minerals. Platinum tubing (5 mm diameter) was cut 1.2 cm long, tri-welded on one end, and annealed before ~300 mg of the LiBaC-mineral mixture was loaded into the capsule. The capsule was welded shut using soaked kimwipe pieces as insulators to prevent the sample from heating significantly during the welding. For experiments in which two samples were run simultaneously (contained in a pyrophyllite crucible), 4 mm diameter Pt tubing was prepared similarly, and ~150 mg of sample was loaded per capsule. Figure 6.1 shows the sample assembly for the LiBaC experiments. A piston-cylinder apparatus (Figure 2.2)

was used to achieve high temperature and pressure conditions for the LiBaC experiments, summarized in Table 6.1. Experiments were run for 2-24 hours (Table 6.1). Once the capsule was recovered after the experiment, it was sawed or filed open.

Post-Experiment Sample Preparation Procedures

Recovered charges from piston-cylinder experiments underwent a series of HCl treatments in a cleanroom in order to separate run product olivines from Li-source carbonate material. The HCl treatment consisted of adding 40 ml HCl to the sample, placing in an ultrasonic bath until carbonate dissolution, centrifuging for 10 minutes at 4000 rpm, then pouring off the acid into a collection container. Five treatment rounds were done using 4N HCl, 4N HCl, 2 N HCl, 0.5N HCl, and Milli-Q water. The collected acid from the centrifuge process was dried down on a hot plate and, when fully evaporated, was picked up in 4N HCl.

For experiments containing both olivine and diopside, run product crystals were mounted in epoxy and polished for *in-situ* analysis. For olivine-only experiments, run product crystals were digested using a multi-acid procedure. Samples were pre-weighed before enduring a series of acid treatments, in which the sample reacted with each acid until fully dissolved, then dried down on a hotplate before addition of the next acid. The acid treatment followed was 3 ml concentrated HF, 4 ml 6N HCl, 4 ml 8N HNO₃, and 3 ml 4N HCl. If a sample did not dissolve by manual shaking, it was placed in an ultrasonic bath to accelerate dissolution.

Column Chemistry and Multi-Collector Inductively Coupled Plasma Mass Spectrometry (MC-ICP-MS)

Column chemistry is necessary to isolate lithium prior to analysis using a multi-collector inductively coupled plasma mass spectrometer (MC-ICP-MS). Column chemistry was conducted at the Isotope Geochemistry Laboratory cleanroom at the University of Maryland. Complete preparation involved four sets of columns. The sample, dissolved in 3ml of 4N HCl, was centrifuged before beginning the column chemistry. The procedures are based on the first three column descriptions from Moriguti and Nakamura (1998a) and Rudnick *et al.* (2004). For each set of columns,

fresh acid was passed through the column (via gravity) to condition the resin prior to sample addition and was collected in a waste beaker. The sample was then passed through the columns and collected. The columns were always rinsed with 6N HCl between samples. After the sample passed through the columns, it sat on a hot plate until evaporation was complete. The sample residue was picked up in 3 ml of 2% HNO₃ in preparation for MC-ICP-MS analysis.

Analysis of lithium concentrations and isotopic compositions by MC-ICP-MS was conducted at the Isotope Geochemistry Laboratory at the University of Maryland. Details regarding the instrument and the procedures for using it can be found in Rudnick *et al.* 2004 and Teng *et al.* 2004. Before analysis, ²³Na/⁷Li ratios were measured semi-quantitatively to ensure that no sample had a ratio > 5, since high Na in sample solutions can cause instrument instability that may result in Li isotope fractionation. Samples having high ratios were passed through the column chemistry once more. An ASX-100® (Cetac Technologies) auto-sampler was used to deliver lithium solutions (~100 ppb Li in 2% HNO₃) to the Ar plasma torch. Samples were passed through an Aridus® (Cetac Technologies) desolvating nebulizer fitted with a PFA spray chamber and micronebulizer (Elemental Scientific). For further analytical details, see Rudnick *et al.* 2004. Samples were analyzed on a Nu Plasma multi-collector ICP-MS. Lithium measurements were bracketed by L-SVEC and in-house standards (UMD-1). The 2σ uncertainty for Li using this instrument is ± 1‰.

Laser Ablation Inductively Coupled Plasma Mass Spectrometer (LA-ICP-MS)

Analyses of Li concentrations were conducted at the Materials Characterization Laboratory at Penn State University using a Thermo Scientific X-Series 2 quadrupole inductively coupled plasma mass spectrometer (ICP-MS). The New Wave UP213 laser ablation system uses a Neodymium-Yttrium-Aluminum-Garnet (Nd-YAG) laser to ablate the sample and He and Ar gas carries the ablated particles to the Ar plasma torch of the ICP-MS. Lithium concentrations were determined, using ²⁶Mg as a normalizing mass, from counts-per-second of ⁷Li using the LasyBoy data reduction spreadsheet described in Chapter 2.4. Laser analyses used a frequency of 10 Hz with spot sizes of 40 μm and an

average output power of 11 J/cm². Sample-standard bracketing with Nist612 and BHVO standards was done to ensure accuracy of the analyses.

Secondary Ion Mass Spectrometer (SIMS)

Analysis of Li concentrations by secondary ion mass spectrometer (SIMS) was conducted at the Pheasant Memorial Laboratory for Geochemistry and Cosmochemistry, Institute for Study of the Earth's Interior at Okayama University, Japan. The Cameca ims-5f SIMS was used with a primary oxygen beam with a primary beam current of 20 nA, primary impact energy of +17 keV, and a secondary accelerating voltage of +4.5 kV. Sample mounts were gold coated before analysis to prevent surface charge buildup. In-house standards were used to ensure accurate results.

6.3 Experimental Results

Lithium Concentrations and Isotope Ratios

Starting materials and run products were analyzed by MC-ICP-MS for Li concentrations and isotope ratios; results of these analyses are presented in Table 6.2. The diopside starting material lithium measurements were reproducible and are accepted as accurate. The olivine starting material measurements have more variation in the reported values for both $\delta^7\text{Li}$ (+2.6 to +8.8) and Li abundances (2 to 5 ppm). The lithium isotope values in the carbonate powder analyses are very heavy ($\delta^7\text{Li} = +80$). These values are typical for commercially supplied lithium materials, which are the residues of ⁶Li extraction for nuclear weapons development. In most cases, $\delta^7\text{Li}$ in residual (run product) carbonate > starting material carbonate > olivine run products.

In Situ Measurement of Li concentrations in Olivine and Diopside

Starting material olivine and diopside and twelve experimental run products were mounted in epoxy, polished, and analyzed for lithium concentrations using LA-ICP-MS (Table 6.3). The Li concentrations in all of the run product olivines are higher than the average Li concentration for the starting material olivines. Contrastingly, the diopside run products look remarkably like the starting materials, suggesting that Li diffusion is slower for diopside. As mentioned in section 6.2, the barium serves as a check for the

system. Analyses having high amounts of barium (> 15 ppm) were considered contaminated with LiBaC source and would therefore give an inaccurate measurement for lithium concentration.

Starting materials and run products of two experiments (Li-11 and Li-14) conducted at 900°C for 4 hours and 24 hours were analyzed by SIMS (Table 6.4). Figure 6.2 is a plot of Li vs. Ba concentrations (ppm) for the olivine and diopside grains contained in the two runs. The starting materials for both the olivine and diopside do not have Ba concentrations exceeding 1 ppm, as would be expected since Ba is not compatible in either mineral structure. Barium concentrations in the run products show a wide variability, ranging from less than 1 ppm to > 1000 ppm. Similarly, lithium concentrations in the run products are highly variable, ranging from < 1 ppm to ~ 700 ppm. As seen in Figure 6.2, high Li concentrations can be correlated with high Ba concentrations.

6.4 Discussion

Approach to Equilibrium

In retrospect, run durations of 2-24 hours were insufficient to approach complete diffusion (i.e. equilibrium) of Li at any experimental temperature. If the minerals were inclusion-free and if equilibrium were approached, the data points would cluster closely in two regions, with the 200 ppm LiBaC run products having a final lithium concentration that is ten times that for the 20 ppm LiBaC run products. For both minerals in Figure 6.2, two distinct clusters of data are not present. Li distribution is very scattered, and the data generally follow a mixing-line trend at high Li and Ba concentrations. Distributions of Li and Ba that follow a mixing-line trend are expected to reflect inclusions of the carbonate flux in the run product minerals.

Partial Melting of Lithium-Barium-Carbonate Flux

The olivine data in Figure 6.2 shows that some diffusion of lithium occurred, evidenced by some points having Li concentrations greater than the starting material even at Ba concentrations < 1 ppm. Most importantly, some olivine grains had Li

concentrations higher than was available in the LiBaC source. The olivine grain having the greatest Li concentration had 707 ppm Li measured, and its LiBaC source only had 200 ppm. My interpretation of this observation is that the LiBaC powder partially melted during the experiment, and the melt became enriched in Li relative to the starting LiBaC powder. Even though the concentration of Li in this partial melt source is unknown, the data follow the general trend of the mixing line, suggesting that the grains contain inclusions of a partial melt whose end-member has much higher Li concentrations than the LiBaC. Many diopside grains have Li concentrations similar to starting material with low Ba contents, suggesting that little diffusion occurred; others follow a mixing line similar to olivine (Figure 6.2).

Carbonate Melt Inclusions in Run Product Minerals

Optical observation of olivine and diopside run products revealed many cracks and inclusions within the olivine and diopside grains (Figure 6.3). Inclusions may explain the trends observed in Figure 6.2, which approximate mixing lines more closely than an equilibrium distribution of Li. In light of the evidence from the SIMS data, the C-ICP-MS analyses likely show the overprint of the included carbonate melt due to the inclusions of LiBaC in the run product grains prior to digestion, which could make the MC-ICP-MS analyses unreliable. Barium concentrations were not acquired from the MC-ICP-MS measurements, so identification of contaminated samples was not possible. Run product analyses by LA-ICP-MS and SIMS having high Ba concentrations (> 15 ppm) were considered contaminated by carbonate melt inclusions.

6.5 Conclusions

Lithium and barium concentrations for run products in Figure 6.2 follow mixing-line trends that do not have the starting carbonate compositions as end-members, which suggests a Li-enriched partial melt of the carbonate flux. The lithium and barium concentration of the partial melt is not known. Lithium concentrations observed for run product olivines and diopside are interpreted to represent some combination of Li incorporated as a lattice component and carbonate melt inclusions, which usually co-vary with Ba and can have Li abundances higher than the LiBaC source. Thus, true lithium

concentrations in the run products are difficult to assess. The results presented here indicate that this experimental method has too much uncertainty to properly determine partition coefficients or isotopic fractionation factors.

Table 6.1. Summary of samples and experimental conditions for LiBaC experiments.

Sample Name	Mineral Inputs	LiBaC # (Li source)	[Li] (ppm)	$\delta^7\text{Li}$ (‰)	Run Duration (hours)	Temperature (°C)	Pressure (GPa)	Run Products
Li-1	ol	1	100	+80	2	1100	1.4	ol
Li-4	ol	1	100	+80	2	1100	1.4	ol
Li-7	ol	2	200	0	2	1100	1.4	ol
Li-2	ol	1	100	+80	4	900	1.4	ol
Li-5	ol	2	200	+80	4	900	1.4	ol
Li-11A	ol, cpx	2	200	0	4	900	1.4	ol, cpx
Li-14A	ol, cpx	2	200	0	4	900	1.4	ol, cpx
Li-11B	ol, cpx	3	20	0	4	900	1.4	ol, cpx
Li-14B	ol, cpx	3	20	0	4	900	1.4	ol, cpx
Li-3	ol	1	100	+80	24	700	1.4	ol
Li-6	ol	2	200	0	24	700	1.4	ol
Li-10A	ol, cpx	2	200	0	24	700	1.4	ol, cpx
Li-10B	ol, cpx	3	20	0	24	700	1.4	ol, cpx

Sample Assembly

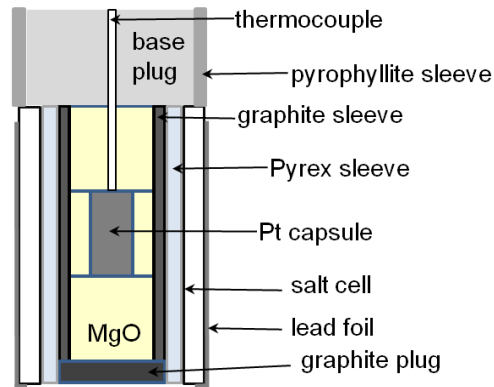


Figure 6.1. Schematic of sample assembly used for LiBaC experiments with the piston-cylinder.

Table 6.2. Summary of MC-ICP-MS analyses for starting materials, run product olivines, and run product CO₃ dissolved in HCl for LiBaC experiments.

Sample	Description	Temperature (°C)	Duration (hours)	Pressure (GPa)	LiBaC δ ⁷ Li (‰)	δ ⁷ Li (‰) ^a	[Li] (ppm) ^b	Notes ^c
<i>Starting Materials</i>								
YO-1	olivine					+6.7	3	
YO-2	olivine					+5.2	4	
MF-3	olivine					+2.6	3	
MF-4	olivine					+8.8	5	
MF-13	olivine (leached in 4N HCl)					+3.7	2	
YD-1	diopside					+9.2	6	
YD-2	diopside					+9.5	6	
MF-1	original LiBaCO ₃				+80	+81.3	87	
MF-2	Li ₂ CO ₃ (heavy)				+80	+80.5	21.2%	
<i>Standards as Unknowns</i>								
UMD-1 ^d	50 ppm Li, δ ⁷ Li = + 54.7					+54.3	53.4	n = 6.
IRMM-016 ^d	100 ppm Li, δ ⁷ Li = -0.1					-0.2	104.8	n = 4.
<i>Run Products</i>								
Li-4	olivine	1100	2	1.4	+80	+75.7	93	RA: 65 ppm, +75.9‰.
Li-1	olivine	1100	2	1.4	+80	+70.4	88	High error.
Li-7	olivine	1100	2	1.4	0	-1.7	63	RA: 60 ppm, -1.4‰.
Li-2	olivine	900	4	1.4	+80	+62.7	86	High error.
Li-5	olivine	900	4	1.4	0	-3.0	65	RA: 103 ppm, -3.3‰.
Li-3	olivine	700	24	1.4	+80	+72.4	44	RA: 64 ppm, +74.2‰.
Li-6	olivine	700	24	1.4	0	+1.3	88	RA: 68 ppm, +1.3‰.
MF-6	CO ₃ from Li-1	1100	2	1.4	+80	+82.6	50	RA: 53 ppm, +82.1‰.
MF-17	CO ₃ from Li-7	1100	2	1.4	0	+3.9	55	
MF-7	CO ₃ from Li-2	900	4	1.4	+80	+87.6	47	RA: 51 ppm, +86.9‰.
MF-15	CO ₃ from Li-5	900	4	1.4	0	+6.7	42	
MF-8	CO ₃ from Li-3	700	24	1.4	+80	+82.4	43	
MF-16	CO ₃ from Li-6	700	24	1.4	0	+1.0	111	

^aEstimated uncertainties are ±1‰.

^bLithium concentrations are in ppm unless otherwise noted.

^cRA = Replicate analysis.

^dStandards ran as samples. Accepted values for UMD-1 and IRMM-016 are published in Rudnick *et al.* (2004). 2σ deviations for δ⁷Li and [Li] are, respectively, 1.50 and 10.4 for UMD-1, and 1.4 and 15.6 for IRMM-016. Percent errors for δ⁷Li and [Li] are, respectively, 0.7% and 7% for UMD-1, and 100.0% and 4.8% for IRMM-016.

Table 6.3. Summary of LA-ICP-MS results for starting materials and run products from LiBaC experiments (2 σ error in parentheses).

Sample	Temperature (°C)	Duration (hours)	Pressure (GPa)	LiBaC [Li] (ppm)	Mean [Li] (ppm)
<i>Starting Materials</i>					
SCO					2 (0.8)
DKD					6 (6)
<i>Olivines</i>					
Li-4	1100	2	1.4	100	29 (24)
Li-12A	1100	2	1.4	200	27 (22)
Li-12B	1100	2	1.4	20	4 (4)
Li-5	900	4	1.4	200	30 (30)
Li-11A-Ol	900	4	1.4	200	22 (30)
Li-11B-Ol	900	4	1.4	20	3 (2)
Li-10A-Ol	700	24	1.4	200	3 (0.2)
Li-10B-Ol	700	24	1.4	20	4 (1.2)
<i>Diopsides</i>					
Li-11A	900	4	1.4	200	6 (2)
Li-11B	900	4	1.4	20	7 (2)
Li-10A	700	24	1.4	200	8 (4)
Li-10B	700	24	1.4	20	6 (4)

Table 6.4. Summary of SIMS results for starting materials and run products from LiBaC experiments (2 σ error in parentheses).

Sample	Temperature (°C)	Run Duration (hours)	Pressure (kbar)	LiBaC [Li] (ppm)	Mean [Li] ($\mu\text{g/g}$)
<i>Starting materials</i>					
DKD					6.1 (3.4)
SCO					1.9 (1.0)
<i>Olivine run products</i>					
Li-11A-Ol	900	4	1.4	200	5.8 (16.4)
Li-11B-Ol	900	4	1.4	20	2.5 (3.6)
Li-14A-Ol	900	24	1.4	20	14.6 (67.8)
Li-14B-Ol	900	24	1.4	20	2.2 (2.4)
<i>Diopside run products</i>					
Li-11A-Di	900	4	1.4	200	6.4 (1.4)
Li-11B-Di	900	4	1.4	20	5.2 (2.0)
Li-14A-Di	900	24	1.4	200	5.7 (3.2)
Li-14B-Di	900	24	1.4	20	5.2 (1.4)

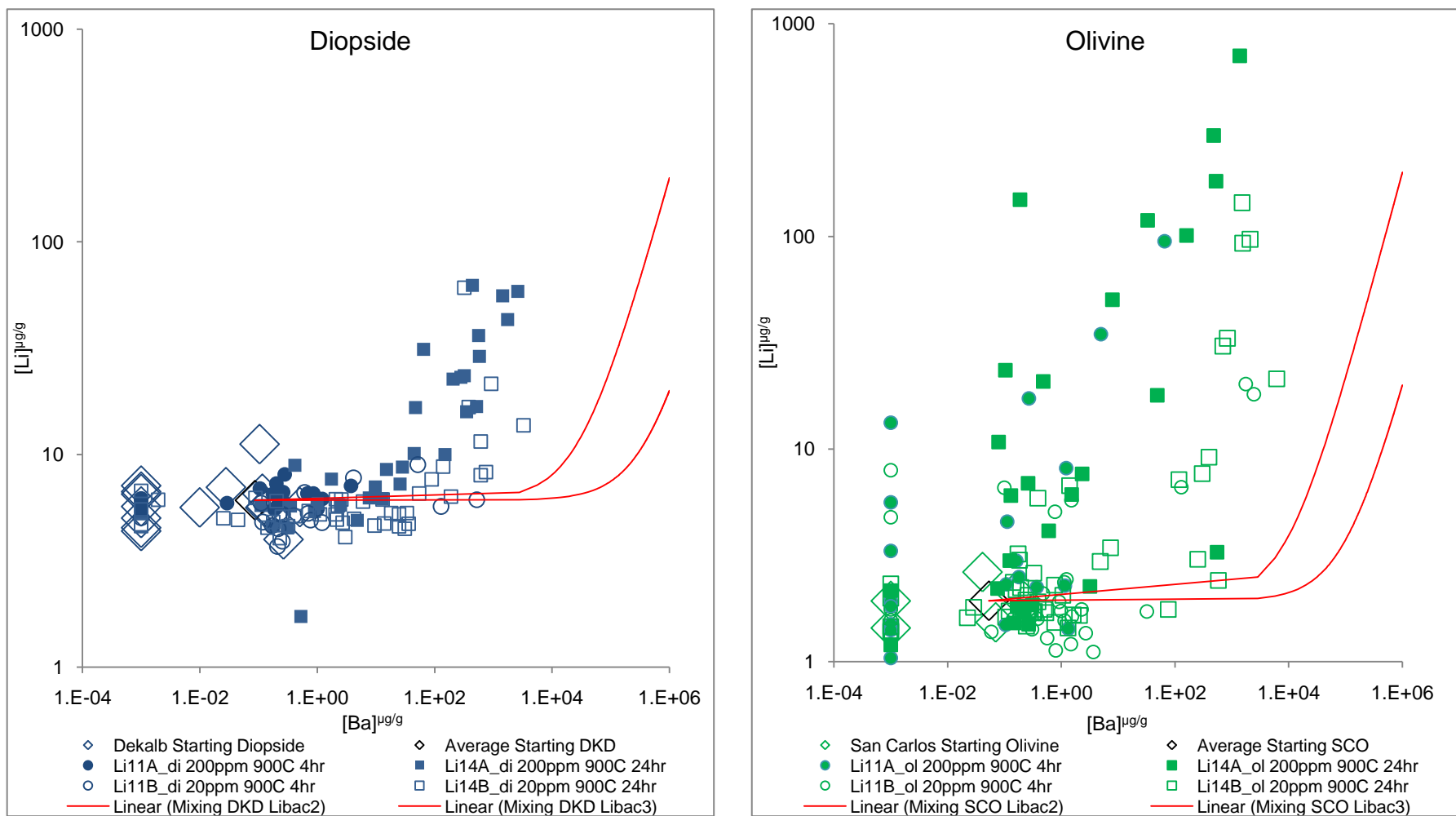


Figure 6.2. Diopside and olivine SIMS results for Li vs. Ba concentrations ($\mu\text{g/g}$). Diopside data presented on left, olivine data presented on right. Open circles and squares represent the experiment that contained 20 ppm Li in the LiBaC powder (LiBaC 3). Closed circles and squares had 200 ppm Li in the LiBaC powder (LiBaC 2). Square symbols represent the 24 hour experiment and circles are the 4 hour experiment. The open diamonds represent analyses of starting material minerals, and the black open diamond represents the average Li and Ba concentrations for the starting materials. The red lines are mixing lines whose end-members are the starting material mineral and the LiBaC powder used for the particular experiment. Inclusions of the LiBaC powder are evidenced by the data points having Ba concentrations greater than 15 ppm. The data do not follow the red mixing curves, but instead indicate interaction with a partial-melt of BaCO_3 and LiCO_3 , for which the Li concentration is not numerically quantified but is much higher than the original powder Li concentration.

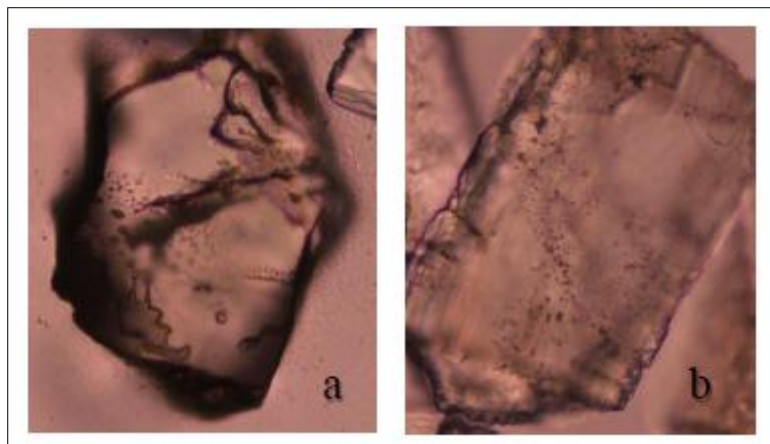


Figure 6.3. Run product images showing cracks and inclusions containing partially molten LiBaC powder in a) olivine and b) diopside.

References

- Ayers, J.C., Brenan, J.B., Watson, E.B., Wark, D.A., Minarik, W.G. (1992) A new capsule technique for hydrothermal experiments using the piston-cylinder apparatus. *American Mineralogist* **77**, 1080-1086.
- Ayers, J.C., Dittmer, S.K., Layne, G.D. (1997) Partitioning of elements between peridotite and H₂O at 2.0-3.0 GPa and 900-1100°C, and application to models of subduction zone processes. *Earth Planet. Sci. Lett.* **150**, 381-398.
- Beattie, P. (1994) Systematics and energetics of trace-element partitioning between olivine and silicate melts: implications for the nature of mineral/melt partitioning. *Chem. Geol.* **117**, 57-71.
- Benton, L.D., Savov, I., Ryan, J.G. (1999) Recycling of subducted lithium in fore-arcs: Insights from a serpentine seamount [abs.]. *Eos (Trans. Amer. Geophys. Union)* **80**, S349.
- Blundy, J. and Dalton, J. (2000) Experimental comparison of trace element partitioning between clinopyroxene and melt in carbonate and silicate systems, and implications for mantle metasomatism. *Contrib. Mineral. Petrol.* **139**, 356-371.
- Blundy, J. and Wood, B. (1994) Prediction of crystal-melt partition coefficients from elastic moduli. *Nature* **372**, 452-454.
- Blundy, J. and Wood, B. (2003) Partitioning of trace elements between crystals and melts. *Earth Planet. Sci. Lett.* **210**, 383-397.
- Boyd, F.R. and England, J.L. (1960) Apparatus for phase-equilibrium measurements at pressures up to 50 kilobars and temperatures up to 1750°C. *J. Geophys. Res.* **65**, 741-748.
- Brenan, J.M., Shaw, H.F., Ryerson, F.J., Phinney, D.L. (1995a) Mineral-aqueous fluid partitioning of trace elements at 900°C and 2.0 GPa: Constraints on the trace element chemistry of mantle and deep crustal fluids. *Geochim. Cosmochim. Acta* **59**, 3331-3350.
- Brenan, J.M., Neroda, E., Lundstrom, C.C., Shaw, H.F., Ryerson, F.J., Phinney, D.L. (1998a) Behavior of boron, beryllium, and lithium during melting and crystallization: Constraints from mineral-melt partitioning experiments. *Geochim. Cosmochim. Acta* **62**, 2129-2141.
- Caciagli-Warman, N. (2010) Experimental constraints on lithium exchange between clinopyroxene, olivine and aqueous fluids at high pressures and temperatures. Unpublished PhD thesis, University of Toronto.

- Chan, L.H., Edmond, J.M., Thompson, G., Gillis, K. (1992) Lithium isotopic composition of submarine basalts: implications for the lithium cycle in the oceans. *Earth Planet. Sci. Lett.* **108**, 151-160.
- Coogan, L.A., Kasemann, S.A., Chakraborty, S. (2005) Rates of hydrothermal cooling of new oceanic upper crust derived from lithium-geospeedometry. *Earth Planet. Sci. Lett.* **240**, 415-424.
- Criss, R.E. and Farquhar, J. (2008) Abundance, notation, and fractionation of light stable isotopes. *Rev. Mineral. Geochem.* **68**, 15-30.
- Dohmen, R., Kasemann, S.A., Coogan, L., Chakraborty, S. (2010) Diffusion of Li in olivine. Part I: Experimental observations and a multi species diffusion model. *Geochim. Cosmochim. Acta* **74**, 274-292.
- Eggins, S.M., Rudnick, R.L., McDonough, W.F. (1998) The composition of peridotites and their minerals: a laser-ablation ICP-MS study. *Earth Planet. Sci. Lett.* **154**, 53-71.
- Filiberto, J., Jackson, C., Le, L., Treiman, A.H. (2009) Partitioning of Ni between olivine and an iron-rich basalt: Experiments, partition models, and planetary implications. *American Mineralogist* **94**, 256-261.
- Gallagher, K. and Elliott, T. (2009) Fractionation of lithium isotopes in magmatic systems as a natural consequence of cooling. *Earth Planet. Sci. Lett.* **278**, 286-296.
- Goldschmidt, V.M. (1937) The principles of distribution of chemical elements in minerals and rocks. 7th Hugo Müller Lecture, delivered before the Chemical Society on March 17th 1937, in *The Principles of Distributions of Chemical Elements, etc.*, 655-673.
- Green, T.H. (1994) Experimental studies of trace-element partitioning applicable to igneous petrogenesis – Sedona 16 years later. *Chem. Geol.* **117**, 1-36.
- Hart, S.R. and Dunn, T. (1993) Experimental cpx/melt partitioning of 24 trace elements. *Contrib. Mineral Petrol.* **113**, 1-8.
- Ionov, D.A. and Seitz, H.M. (2008) Lithium abundances and isotopic compositions in mantle xenoliths from subduction and intra-plate settings: Mantle sources vs. eruption histories. *Earth Planet. Sci. Lett.* **266**, 316-331.
- Jeffcoate, A.B., Elliot, T., Kasemann, S.A., Ionov, D., Cooper, K., Brooker, R. (2007) Li isotope fractionation in peridotites and mafic melts. *Geochim. Cosmochim. Acta* **71**, 202-218.

- Leeman, W.P., Tonarini, S., Chan, L.H., Borg, L.E. (2004) Boron and lithium isotopic variations in a hot subduction zone – the southern Washington Cascades. *Chem. Geol.* **212**, 101-124.
- Lifshitz, I.M. and Slyozov, V.V. (1961) The kinetics of precipitation from supersaturated solid solutions. *J. Phys. Chem. Solids* **19**, 35-50.
- McIntire, W.L. (1963) Trace element partition coefficients – a review of theory and applications to geology. *Geochim. Cosmochim. Acta* **27**, 1209-1264.
- Moriguti, T. and Nakamura, E. (1998a) High-yield lithium separation and the precise isotopic analysis for natural rock and aqueous samples. *Chem. Geol.* **145**, 91-104.
- Northrop, D.A. and Clayton, R.N. (1966) Oxygen-isotope fractionations in systems containing dolomite. *J. Geol.* **74**, 174-196.
- O'Neill, H.St.C. and Eggins, S.M. (2002) The effect of melt composition of trace element partitioning: an experimental investigation of the activity coefficients of FeO, NiO, CoO, MoO₂ and MoO₃. *Chem. Geol.* **186**, 151-181.
- Onuma, N., Higuchi, H., Wakita, H., Nagasawa, H. (1968) Trace element partition between two pyroxenes and the host lava. *Earth Planet. Sci. Lett.* **5**, 47-51.
- Paquin, J. and Altherr, R. (2002) Subduction-related lithium metasomatism during exhumation of the Alpe Arami ultrahigh-pressure garnet peridotite (Central Alps, Switzerland). *Contrib. Mineral. Petrol.* **143**, 623-640.
- Parkinson, I.J., Hammond, S.J., James, R.H., Rogers, N.W. (2007) High-temperature lithium isotope fractionation: Insights from lithium isotope diffusion in magmatic systems. *Earth Planet. Sci. Lett.* **257**, 609-621.
- Potts, P.J., Tindle, A.G., Webb, P.C. (1992) *Geochemical Reference Material Compositions*. Whittles, Caithness, Scotland. 313 pp.
- Richter, F.M., Davis, A.M., DePaolo, D.J., Watson, E.B. (2003) Isotope fractionation by chemical diffusion between molten basalt and rhyolite. *Geochim. Cosmochim. Acta* **67**, 3905-3923.
- Rudnick, R.L. and Ionov, D.A. (2007) Lithium elemental and isotopic disequilibrium in minerals from peridotite xenoliths from far-east Russia: Product of recent melt/fluid-rock reaction, *Earth Planet. Sci. Lett.* **256**, 278-293.
- Rudnick, R.L., Tomascak, P.B., Njo, H.B., Gardner, L.R. (2004) Extreme lithium isotopic fractionation during continental weathering revealed in saprolites from South Carolina. *Chem. Geol.* **212**, 45-57.
- Ryan, J.G. and Langmuir, C.H. (1987) The systematic of lithium abundances in young volcanic rocks. *Geochim. Cosmochim. Acta* **51**, 1727-1741.

- Schneider, M.E. and Eggler, D.H. (1986) Fluids in equilibrium with peridotite minerals: Implications for mantle metasomatism. *Geochim. Cosmochim. Acta* **50**, 711-724.
- Seitz, H-M. and Woodland, A.B. (2000) The distribution of lithium in peridotitic and pyroxenitic mantle lithologies – an indicator of magmatic and metasomatic processes. *Chem. Geol.* **166**, 47-64.
- Seitz, H-M., Brey, G.P., Lahaye, Y., Durali, S., Weyer, S. (2004) Lithium isotopic signatures of peridotite xenoliths and isotopic fractionation at high temperatures between olivine and pyroxenes. *Chem. Geol.* **212**, 163-177.
- Shannon, R.D. (1976) Revised effective ionic radii and systematic studies of interatomic distances in halides and chalcogenides. *Acta Cryst.* **A32**, 751-767.
- Steeffel, C.I. and Van Cappellen, P. (1990) A new kinetic approach to modeling water-rock interaction: The role of nucleation, precursors, and Ostwald ripening. *Geochim. Cosmochim. Acta* **54**, 2657-2677.
- Suzuki, T. and Akaogi, M. (1995) Element partitioning between olivine and silicate melt under high pressure. *Phys. Chem. Minerals* **22**, 411-418.
- Tang, Y-J., Zhang, H-F., Ying, J-F. (2007) Review of the lithium isotope system as a geochemical tracer. *Internat. Geol. Rev.* **49**, 674-688.
- Taura, H., Yurimoto, H., Kurita, K., Sueno, S. (1998) Pressure dependence on partition coefficients for trace elements between olivine and the coexisting melts. *Phys. Chem. Minerals* **25**, 469-484.
- Teng, F.Z., McDonough, W.F., Rudnick, R.L., Dalpe, C., Tomascak, P.B., Chappell, B.W., Gao, S. (2004) Lithium isotopic composition concentration of the upper continental crust. *Geochim. Cosmochim. Acta* **68**, 4167-4178.
- Teng, F-Z., Rudnick, R.L., McDonough, W.F., Gao, S., Tomascak, P.B., Liu, Y. (2008) Lithium isotopic composition and concentration of the deep continental crust. *Chem. Geol.* **255**, 47-59.
- Tomascak, P.B. (2004) Developments in understanding and application of lithium isotopes in the Earth and planetary sciences. *Rev. Mineral. Geochem.* **55**, 153-195.
- Tomascak, P.B., Lynton, S.J., Krogstad, E.J., Walker, R.J. (1995) Li isotopes: A new tool for investigating pegmatite petrogenesis. *Geol. Soc. Amer. Abst. Prog.* **27**, 411 (abstr.).
- Tomascak, P.B., Tera, F., Helz, R.T., Walker, R.J. (1999a) The absence of lithium isotope fractionation during basalt differentiation: New measurements by multicollector sector ICP-MS. *Geochim. Cosmochim. Acta* **63**, 907-910.

- Tomascak, P.B., Ryan, J.G., Defant, M.J. (2000) Lithium isotope evidence for light element decoupling in the Panama subarc mantle. *Geology* **28**, 507-510.
- Tomascak, P.B., Langmuir, C.H., le Roux, P.J., Shirey, S.B. (2008) Lithium isotopes in global mid-ocean ridge basalts. *Geochim. Cosmochim. Acta* **72**, 1626-1637.
- White, W.M. (2009) Geochemistry. *Online textbook, Internat.Mine Water Assoc.*
<http://www.imwa.info/geochemistry/>.
- Wood, B.J. and Blundy, J.D. (2001) The effect of cation charge on crystal-melt partitioning of trace elements. *Earth Planet. Sci. Lett.* **188**, 59-71.
- Woodland, A.B., Seitz, H.M., Yaxley, G.M. (2004) Varying behavior of Li in metasomatised spinel peridotite xenoliths from western Victoria, Australia. *Lithos* **75**, 55-66.
- Zack, T., Tomascak, P.B., Rudnick, R.L., Dalpé, C., McDonough, W.F. (2003) Extremely light Li in orogenic eclogites: The role of isotope fractionation during dehydration in subducted oceanic crust. *Earth Planet. Sci. Lett.* **208**, 279-290.
- Zanetti, A., Tiepolo, M., Oberti, R., Vannucci, R. (2004) Trace-element partitioning in olivine: modeling of a complete data set from a synthetic hydrous basanite melt. *Lithos* **75**, 39-54.